Simulations of Nematic Liquid Crystals: Confined Geometries, Phase Transitions and Topological Defects

by

Nikolai V. Priezjev

B.Sc., Moscow Institute of Physics and Technology, 1997
Sc.M., Brown University 1999

Thesis

Submitted in partial fulfillment of the requirements for
the Degree of Doctor of Philosophy
in the Department of Physics at Brown University

May 2002

Abstract of “Simulations of Nematic Liquid Crystals: Confined Geometries, Phase Transitions and Topological Defects,” by Nikolai V. Priezjev, Ph.D., Brown University, May 2002

The physics of liquid crystals is an exciting field of research with important practical applications. In this dissertation we present the results of simulation studies of nematic liquid crystals using Monte Carlo and molecular dynamic techniques. In our first project we performed Monte Carlo simulations of the Lebwohl-Lasher (LL) model of nematic liquid crystals confined to cylindrical cavities with perpendicular anchoring. In this particular geometry one has an interesting interplay between bulk and surface energies, which results in different director configurations inside the cylinder. Our work reconciled the apparent contradictions between the results of earlier simulations and approximate analytic theories. In another project we simulated the nematic–isotropic transition in the LL model using a single cluster Monte Carlo algorithm. We calculated the finite size scaling of the free energy barrier at the transition and obtained a reliable estimate of the value of the transition temperature in the thermodynamic limit for the first time. We also used the cluster algorithm to study the behavior of disclination loop defects in the vicinity of the nematic–isotropic transition in the LL and related models. We calculated the distribution of these defects and were able to draw interesting conclusions about their behavior at the transition, and contrast the behavior with analogous magnetic systems. In our last project we studied the coarsening dynamics of biaxial nematics using Langevin molecular dynamics. We used a model with no a priori realtionship among the three elastic constants associated with director deformations. We found a rich variety of coarsening behavior, including the simulataneous decay of nearly equal populations of the three classes of half–integer disclination lines. The behavior we observed can be understood on the basis of the relative values of the elastic constants and the resulting decay channels of the defects.

This dissertation by Nikolai V. Priezjev is accepted in its present form by
the Department of Physics as satisfying the
dissertation requirement for the degree of
Doctor of Philosophy

Date............................ ....
Robert A. Pelcovits, Adviser

Recommended to the Graduate Council

Date............................ ....
Michael J. Kosterlitz, reader

Date............................ ....
Gregory P. Crawford, reader

Approved by the Graduate Council

Date............................ ....
Peder J. Estrup
Dean of Graduate School and Research

The Vita of Nikolai V. Priezjev

Nikolai V. Priezjev was born on the 7 of April 1975 in the city of Dubna, Moscow Region, Russia. Nikolai graduated with a B.Sc. degree in Physics from Moscow Institute of Physics and Technology in 1997. He entered the graduate program of the Physics Department at Brown University in the Fall of 1997 and earned his Master of Science degree in May 1999. During his graduate studies at Brown University, he worked as a teaching assistant, research assistant and was a recipient of the Dissertation Keen Fellowship from the Brown University Graduate School. His research has been focused on Soft Condensed Matter Theory, in particular liquid crystals.

This work was supported in part by National Science Foundation under grant DMR–9873849. For the past year the financial support has been provided me by Dissertation Keen Fellowship from Graduate School at Brown University. Computations were carried out at the Theoretical Physics Computing Facility at Brown University.

Contents

List of Tables

List of Figures

Chapter 1

Introduction and Overview

1.1 Liquid Crystal Phases

A liquid crystal molecule (or mesogen) is anisotropic in shape. A simplified view of liquid crystal molecules is rod–like object which have both orientational and translational degrees of freedom. The schematic representation of common liquid crystal phases is shown on Fig. (1.1). At high temperatures an isotropic (disordered) phase is formed with absence of translational and orientational long range orders. The liquid crystal in isotropic phase behaves like a fluid and looks transparent in a daylight. With a decrease in temperature, the orientationally ordered *nematic phase* develops while the centers of the mass of the molecules are still distributed random in space. However the long axes are aligned on average, leading to long range orientational order. The average direction of alignment is refered as the *director* $\hat{\mathbf{n}}$ [1] as shown on Fig. (1.1). The word "nematic" originates from Greek ($\nu\eta\mu\alpha$) which means thread. This name was given by G. Friedel [2] who observed the thread–like textures associated with topological defects in nematics when seen under crossed polarizers of an optical microscope. The phase transition from nematic to isotropic phase is a weakly first order one [3]. Sometimes the transition temperature is called a "clearing point" because nematic phase appears milky.

Nematic liquid crystals have very *important symmetry* that both directors $\hat{\mathbf{n}}$ and $-\hat{\mathbf{n}}$ correspond

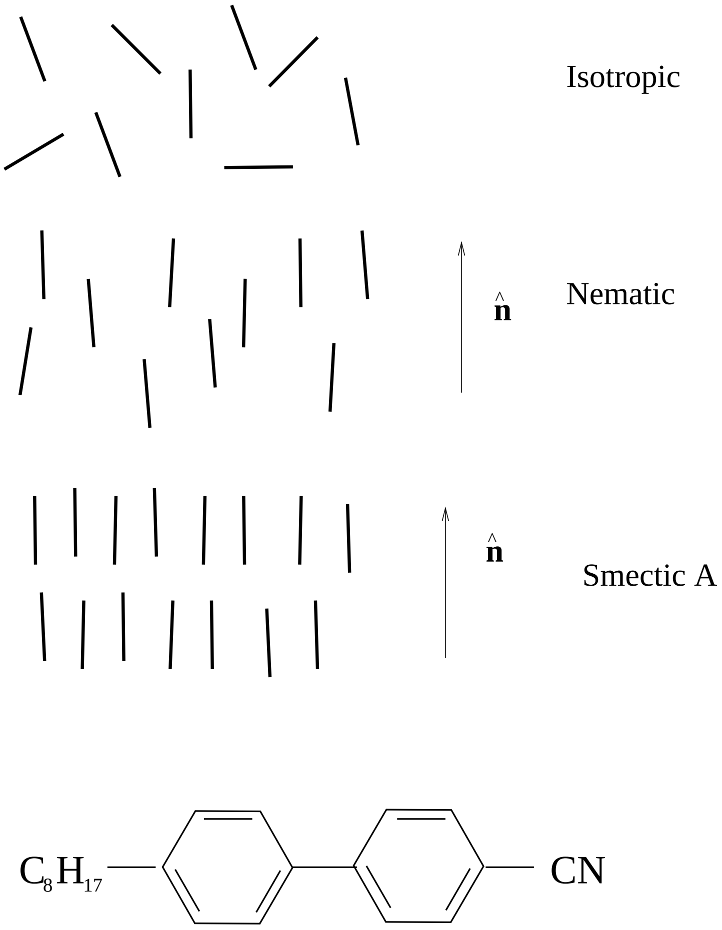

Figure 1.1: Schematic illustration of isotropic, nematic and smectic A liquid crystals phases. Here rods represent the long axes of the molecules. An example molecule of 8CB is shown on the bottom of the figure. It consists of two benzene rings and two terminal groups.

to the same physical state. In particular this symmetry implies that the elastic free energy of the nematics should be proportional to the gradient of $\mathbf{\hat{n}}$ squared. The elastic theory of curvature distortions for nematic liquid crystals was developed by Oseen [5] and Frank [6]. In the absence of an applied magnetic field, the elastic free energy density is given by the following equation:

$$F_{Frank} = \frac{1}{2}\,[k_{11}(\nabla \cdot \mathbf{\hat{n}})^{\mathbf{2}} + \mathbf{k_{22}}(\mathbf{\hat{n}} \cdot \nabla \times \mathbf{\hat{n}})^{\mathbf{2}} + \mathbf{k_{33}}(\mathbf{\hat{n}} \times (\nabla \times \mathbf{\hat{n}}))^{\mathbf{2}}] \tag{1.1}$$

where k_{11}, k_{22} and k_{33} are the three Frank elastic constants associated with splay, twist and bend distortions, respectively. These characteristic deformations are illustrated on Fig. (1.2). Note that each term yields the same energy for $\mathbf{\hat{n}}$ and $-\mathbf{\hat{n}}$ as required for the symmetry of the nematic. In many cases it is helpful to use further approximation for the Frank free energy Eq. (1.1), namely to assume the elastic isotropy associated with splay, twist and bend distortions. In one constant approximation $k = k_{11} = k_{22} = k_{33}$ the free energy density takes form:

$$F_d = \frac{1}{2}k\,[(div\mathbf{\hat{n}})^{\mathbf{2}} + (\mathbf{curl}\mathbf{\hat{n}})^{\mathbf{2}}] = \frac{\mathbf{1}}{\mathbf{2}}\mathbf{k}\ \partial_\alpha \mathbf{n}_\beta\ \partial^\alpha \mathbf{n}^\beta = \frac{\mathbf{1}}{\mathbf{2}}\mathbf{k}\,\left[\left(\frac{\partial \mathbf{\hat{n}}}{\partial \mathbf{x}}\right)^{\mathbf{2}} + \left(\frac{\partial \mathbf{\hat{n}}}{\partial \mathbf{y}}\right)^{\mathbf{2}} + \left(\frac{\partial \mathbf{\hat{n}}}{\partial \mathbf{z}}\right)^{\mathbf{2}}\right] \tag{1.2}$$

The order parameter for nematic liquid crystals is a tensor which respect the symmetry $\mathbf{\hat{n}}$ to $-\mathbf{\hat{n}}$ and it is defined by:

$$Q_{\alpha\beta} = \frac{1}{2N}\Big(\sum_i [3\ u_{i\alpha}u_{i\beta} - \delta_{\alpha\beta}]\Big) \tag{1.3}$$

where the sum is over all molecules and α, β are summed over x, y and z. The tensor $Q_{\alpha\beta}$ is symmetric and traceless by construction, since $u_{i\alpha}u_{i\beta} = 1$. In the computer simulations [4] the tensor $Q_{\alpha\beta}$ is diagonalized and its largest eigenvalue S and corresponding eigenvector (director) $\mathbf{\hat{n}}$ are computed. When $Q_{\alpha\beta}$ is multiplied by $\mathbf{\hat{n}}$ from both sides $u_\alpha Q_{\alpha\beta} u_\beta$, the degree of alignment S can be rewritten in the following form:

$$S = \frac{1}{2N}\Big(\sum_i [3(\mathbf{\hat{u}_i} \cdot \mathbf{\hat{n}})^{\mathbf{2}} - \mathbf{1}]\Big) \tag{1.4}$$

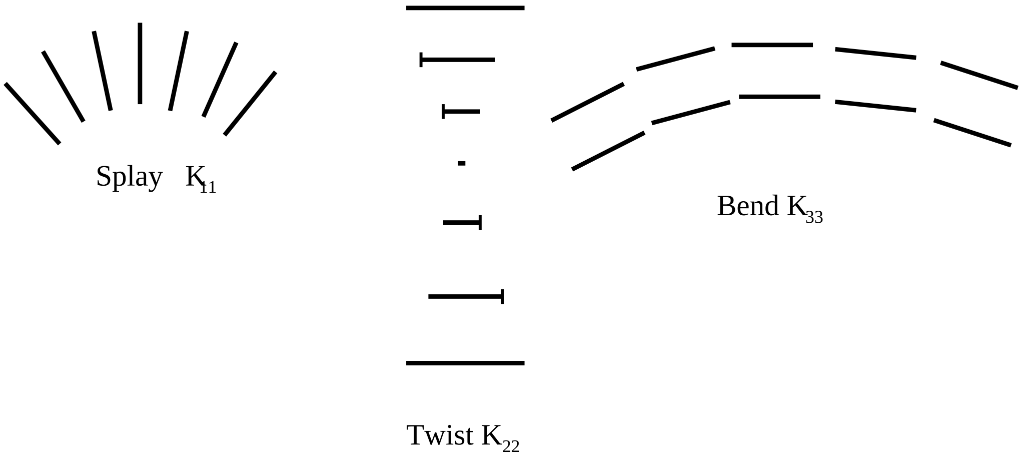

Figure 1.2: Schematic illustration of splay, twist and bend distortions of a nematic liquid crystal. The heads of the "nails" represent the rotation of the molecules out of the plane of the page for twist deformation.

The value of S is a measure of degree of order in the system: it varies from 0 in the isotropic phase to 1 in a perfectly ordered sample.

Upon further cooling down, the translational symmetry of the nematic phase gets broken leading to density modulations in one dimension. In smectic phase Fig. (1.1) molecules tend to aggregate into layers with well defined equilibrium positions and spacings. Within the layers the center of mass of molecules could be random (Smectic A) or have long range hexagonal (orientational) order (Smectic B). In smectic C phase each layer is still a two dimensional liquid but molecules tilted with respect to the normal to the layers. Sometimes smectic liquid crystals are called one–dimensional solid. But the name itself comes again from Greek ($\sigma\mu\eta\gamma\mu\alpha$ = soap) and it was given because certain mechanical properties of smectics reminiscent to the ones of usual soap. The elastic energy for a smectic was derived in the 1930's by Landau and Peierls:

$$F = \frac{1}{2}[B(\nabla_{||}u)^2 + K_{11}(\nabla_{\perp}^2 u)^2] \qquad (1.5)$$

where first term is associated with dilatation (compression) of the layers and second one corresponds to splay distortion of the director at constant layer spacing. Here u describes the displacement field with respect to the ground state of uniform layers. However the smectic free energy Eq. (1.5) is not rotationally invariant. The lowest order correction to the first term in compression energy will be

$\frac{1}{2}B\left[\nabla_{||}u - \frac{1}{2}(\nabla_{\perp}u)^2\right]^2$. This additional non–linear term leads to a buckling instability in a stretched smectic and to fluctuations that normalize compression constant B to zero and splay constant K_{11} to infinity in three dimensional system [7].

1.2 Lebwohl–Lasher Model

The Lebwohl–Lasher (LL) model is the lattice version of the Maier–Saupe model for nematics with an orientational order–disorder transition. While it neglects the coupling between the orientational and translational degrees of freedom present in a real nematic liquid crystal, it is generally believed that this coupling does not play a significant role at the nematic–isotropic (NI) transition. With the absence of translational degrees of freedom the LL model is particularly well–suited for large–scale simulations of the transition. The model is defined by the following Hamiltonian:

$$\mathcal{H} = -\epsilon \sum_{<ij>} P_2(\hat{\mathbf{n}}_i \cdot \hat{\mathbf{n}}_j) = -\epsilon \sum_{<ij>} \left\{ \frac{3}{2} \left(\hat{\mathbf{n}}_i \cdot \hat{\mathbf{n}}_j \right)^2 - \frac{1}{2} \right\} \tag{1.6}$$

where the sum is over all nearest–neighbors, ϵ is a coupling parameter and P_2 is the second Legendre polynomial. The long axes of the rotors are specified by unit vectors $\hat{\mathbf{n}}_{\mathbf{i}}$ and represents a group of approximately 10 molecules. The LL potential Eq. (1.6) is a lattice version of Frank elastic energy Eq. (1.2) in one–constant approximation ($k_{11} = k_{22} = k_{33}$). The LL model has been intensively investigated using Monte Carlo techniques since its introduction [9, 10, 11, 12, 13, 14, 18]. The most complete numerical analysis of the NI transition in the LL model using the conventional single spin flip Metropolis algorithm was carried out by Zhang *et al.* [13] on systems up to a size of 28^3. However, the single spin flip algorithm is inefficient in the critical region and during the course of a simulation the system becomes trapped in one of the local minima corresponding to either the ordered or disordered phases. This difficulty can be overcome by using a cluster algorithm which is most efficient in the critical region and the system samples both local minima effectively. The first such algorithm for nematic liquid crystals was introduced by Kunz and Zumbach [16] to study the two–dimensional LL model. Their algorithm is a modification of the Wolff algorithm [15] for ferromagnetic systems, and greatly reduces critical slowing down. In our earlier publication [18], which we discuss in great details in Chapter 3, we used the Kunz–Zumbach algorithm to carry out a finite–size scaling analysis of the NI transition in the three–dimensional LL model with systems sizes up to 70^3 using the Ferrenberg–Swendsen reweighting technique [17].

1.3 Topological Defects in Nematic Liquid Crystals

Topological defects play an important if not determining role in such phenomena as the structure in confined geometries (Chapter 2), the nature of phase transitions (Chapters 3-4), or the approach to equilibrium after a quench into an ordered state (Chapter 5). In this Chapter we give basic definitions of topological defects in nematic liquid crystals which are disclination lines and monopoles.

For simplicity let us consider a planar structure where director is confined to the xy plane and z independent. Taking the director components $n_x = cos\phi, n_y = sin\phi, n_z = 0$ and writing the free energy density in one constant approximation, the equation (1.2) reduces to the following simple form:

$$F_d = \frac{1}{2}\ k\ (\nabla\phi)^2 \tag{1.7}$$

The non–trivial solutions of this equation are:

$$\phi = s\alpha + c \tag{1.8}$$

where $\alpha = tan^{-1}(y/x)$, c represents a constant phase and s could be any half–integer:

$$s = \pm\frac{1}{2},\ \ \pm 1,\ \ \pm\frac{3}{2},\ ... \tag{1.9}$$

The singular disclination line runs parallel to z axis and the director orientation changes by $2\pi s$ around the core of the line. s is known as the *strength* of the disclination. In Fig. (1.3) we show a few examples of singular configurations for various values of s and c in xy plane . To visualize three

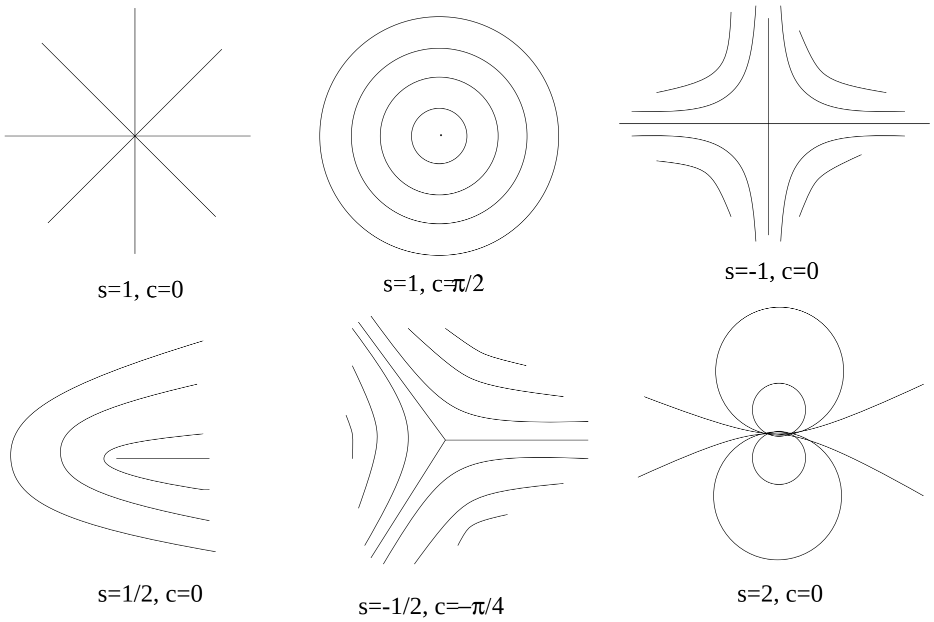

Figure 1.3: Examples of the director configurations around defects with various strengths s and phases c, see Eq. (1.8). Note the difference between top left and top right vortices. In the first case the director rotates clockwise around the core ($s = 1$) unlike the later case where there is anti-clockwise rotation $s = -1$ of the director. And these vortices *can not* be transformed into each other by simply rotating the overall phase, unlike the top left and middle vortices.

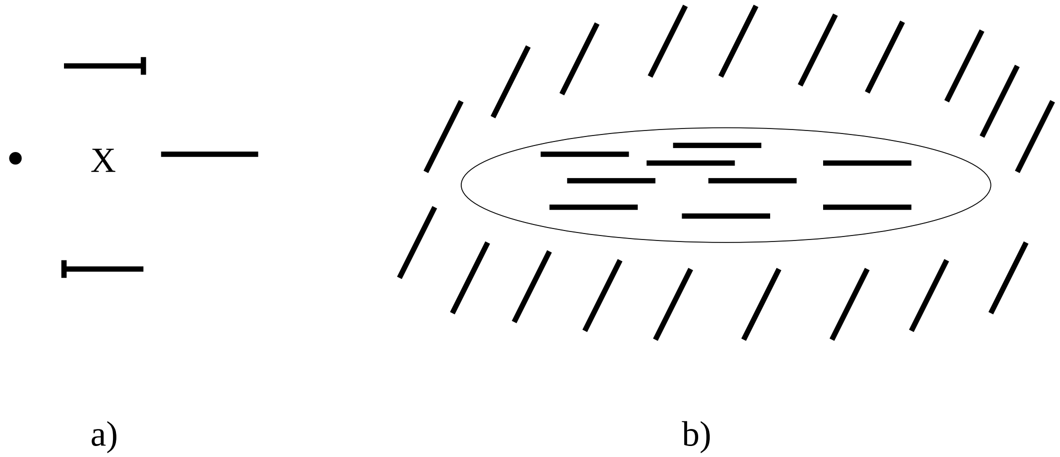

Figure 1.4: a) Director configuration around the core of a twist disclination line (marked by the cross); heads of the "nails" shows the rotation of the molecules out of the plane of the page. To the left of the defect, the director is parallel to the line and perpendicular to plane of the page. On a right side the director is perpendicular to the disclination line and lies in the plane of the page. b) Schematic presentation of the director orientation inside and out of the twist disclination loop. The region inside the twist loop has an uniform orientation and rotates by 90° with respect to exterior director orientation.

dimensional disclination lines one can imagine extending the planes shown in the Fig. (1.3) into and out of the page. Constructed in such a way the $s = \pm\frac{1}{2}$ line is called a *wedge* disclination and $s = \pm 1$ is refered as *type–1* disclination line. In a large enough sample type–1 line can reduce its energy by escaping in third dimension and form non–singular configuration Fig. (1.6), sometimes called *escaped radial* configuration. We discuss in great details in the next Chapter the different conditions required for obtaining either escaped radial or type–1 lines in confined geometries. Another type of three dimensional line defect is so called *twist* disclination line which is shown schematically on Fig. (1.4a). In the twist line the director rotates out of the plane of the page by 180° around the core of the line.

The order parameter space for nematic liquid crystal is the two-dimensional projective plane RP^2, which can be visualized simply as a unit sphere with antipodal (opposite) points identified [19]. Any stable $\frac{1}{2}$ disclination (wedge or twist) could be represented as a noncontractible path on the order parameter space that connects two opposite points. All other half–integer valued lines, whether positive or negative, can be continuously deformed to a line with charge $+\frac{1}{2}$, and integer–valued lines can "escape in the third dimension" [19].

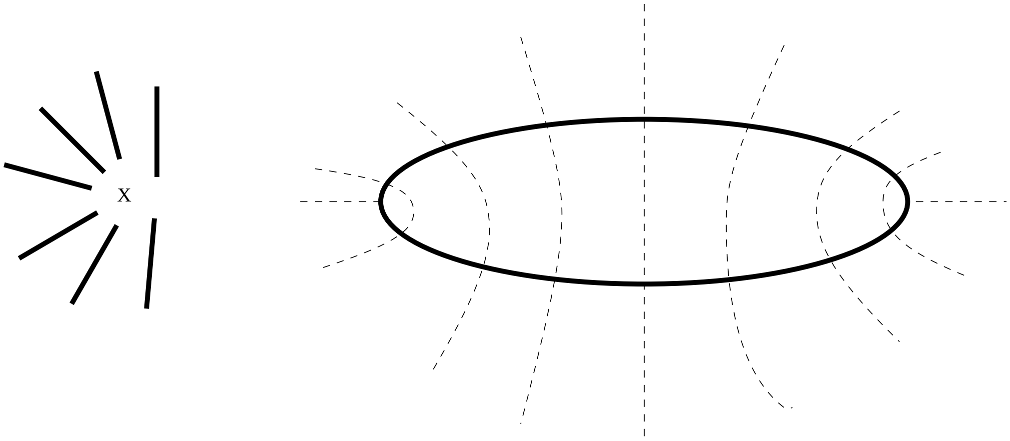

a)

b)

Figure 1.5: a) Director configuration around the core of the wedge disclination line (marked by the cross). The director rotates by 180° in the plane perpendicular to the disclination line. b) The radial configuration of the director (shown by the dashed line) around the wedge disclination loop.

In the bulk, disclinations can form either closed loops (because of a large energy cost associated with having a free end) or terminate on the boundaries. The examples of twist and wedge loops are illustrated on Fig. (1.4b) and Fig. (1.5b) respectively. The main difference between these two configurations is that wedge loop has a net *monopole* charge Eq. (1.10) when seen from a distance larger than its radius. While twist loops do not carry a net charge and thus appear uniform at large distances. In general, monopole charge of a point (or a loop) can be defined as an integral of a flux going through the enclosed surface:

$$q = \frac{1}{8\pi} \int dS_i \; \epsilon_{ijk} \; \mathbf{n} \cdot (\partial_{\mathbf{j}} \mathbf{n} \times \partial_{\mathbf{k}} \mathbf{n}) \tag{1.10}$$

where the charge of the monopole q could be any positive integer. In the Chapter 4 we explore the question of locating the point monopoles in the vicinity of the nematic–isotropic phase transition. We also study the distribution of disclination loops above, below and at the transition and extract their integer monopole charge.

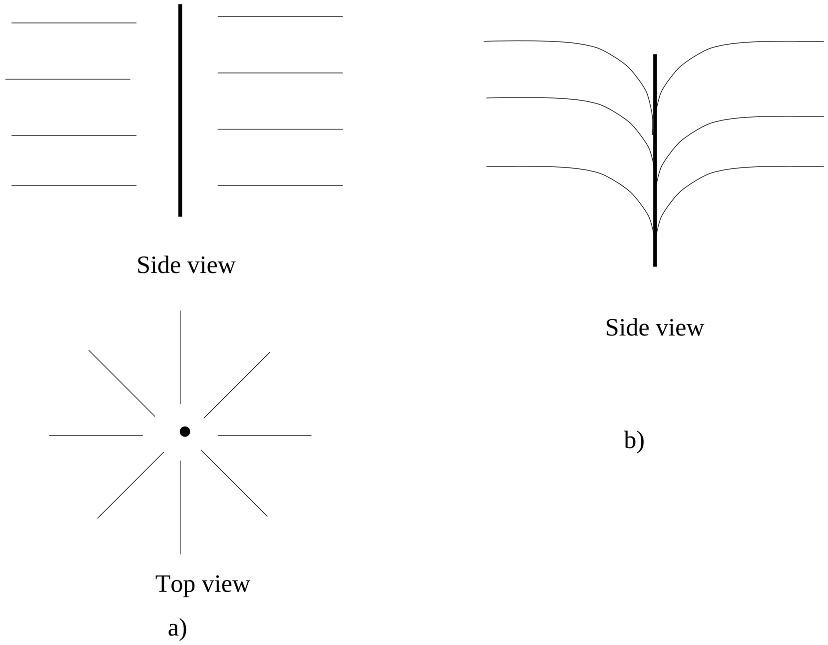

Figure 1.6: a) Side and top views of singular disclination line of unit charge. Director rotates by 360° around the core of the line. b) Escaped Radial non–singular configuration is shown.

Bibliography

[1] P. de Gennes and J. Prost, *The Physics of Liquid Crystals* (Clarendon Press, Oxford, 1993).

[2] G. Friedel, Ann. Physique **18,** 273 (1922).

[3] P. M. Chaikin and T. C. Lubensky, *Principles of Condensed Matter Physics* (Cambridge University Press, Cambridge, 1995).

[4] M. P. Allen and D. J. Tildesley, *Computer Simulations of Liquids* (Claredon, Oxford, 1987).

[5] C. W. Oseen, Trans. Faraday Soc., **29,** 883 (1933).

[6] F. C. Frank, Discuss. Faraday Soc., **25,** 19 (1958).

[7] G. Grinstein and R. A. Pelcovits, Phys. Rev. Lett. **47,** 856 (1981).

[8] P. A. Lebwohl and G. Lasher, Phys. Rev. A **6,** 426 (1972).

[9] G. R. Luckhurst and P. Simpson, Mol. Phys. **47,** 251 (1982).

[10] U. Fabbri and C. Zannoni, Mol. Phys. **4,** 763 (1986).

[11] F. Biscarini, C. Zannoni, C. Chiccoli, and P. Pasini, Mol. Phys. **73,** 439 (1991).

[12] C. Zannoni, J. Chem. Phys. **84,** 424 (1986).

[13] Z. Zhang, O. G. Mouritsen, and M. J. Zuckermann, Phys. Rev. Lett. **69,** 1803 (1992); Z. Zhang, M. J. Zuckermann, and O. G. Mouritsen, Mol. Phys. **80,** 1195 (1993).

[14] S. Boschi, M. P. Brunelli, C. Zannoni, C. Chiccoli, and P. Pasini, Int. J. Mod. Phys. C **8,** 547 (1997).

[15] U. Wolff, Phys. Rev. Lett. **62,** 361 (1989).

[16] H. Kunz and G. Zumbach, Phys. Lett. B **257,** 299 (1991); Phys. Rev. B **46**, 662 (1992). See also, S. Caracciolo, R. G. Edwards, A. Pelissetto and A. D. Sokal, Nuc. Phys. B **403,** 475 (1993).

[17] A. M. Ferrenberg and R. H. Swendsen, Phys. Rev. Lett. **61,** 2635 (1988).

[18] N. V. Priezjev and R. A. Pelcovits, Phys. Rev. E **63,** 062702 (2001),
N. V. Priezjev and R. A. Pelcovits, Phys. Rev. E **64,** 031710 (2001).

[19] N. D. Mermin, Rev. Mod. Phys. **51,** 591 (1979).

Chapter 2

Nematics Confined to the Capillary

In this chapter we describe the results of Monte Carlo simulations of the Lebwohl–Lasher model of nematic liquid crystals confined to cylindrical cavities with homeotropic (perpendicular) anchoring. We show that the ratio of the bulk to surface couplings is not in general equal to the corresponding parameter K/W used in elastic theory (where K is the Frank elastic constant in the one constant approximation and W is the surface anchoring strength). By measuring the temperature dependence of K/W (which is equivalent to the surface extrapolation length) we are able to reconcile the results of our simulations as well as others with the predictions of elastic theory. We find that the rate at which we cool the system from the isotropic to nematic phase plays a crucial role in the development of the final director structure, because of a large free energy barrier separating different director structures as well as the temperature dependence of K/W. With a suitably fast cooling rate we are able to keep the system out of a metastable planar state and form an escaped radial structure for large enough systems.

2.1 Nematic Liquid Crystals in Confined Geometries

The properties of nematic liquid crystals in confined geometries continues to be an interesting problem for both basic science and technological reasons [1]. Nematics confined to cylindrical cavities with homeotropic radial boundary conditions can exhibit a variety of nontrivial structures depending on the competition between bulk elastic and surface energies. By minimizing the Frank elastic free energy Cladis and Kleman [2] and Meyer [3] showed that for a cylinder with a sufficiently large radius an escaped radial (ER) configuration will form. They found based on elastic theory that the angle that spins make with the cylinder axis is given by:

$$\theta(r) = 2 \cdot tan^{-1}\left(\frac{r}{R}\right) \tag{2.1}$$

where R is the radius of the cylinder and r is the distance from the axis. Consequently the free energy, which includes only splay and bend deformations will be:

$$F = 3\ \pi K \tag{2.2}$$

where K is a coupling in one–constant approximation. Note that we put all the surface elastic constants to zero $K_{24} = K_{13} = 0$. This configuration can be thought of as a planar radial (PR) structure (i.e. a disclination line) which has "escaped" along the axis of the cylinder (see Fig. 2.1). Later studies [4] showed the possibility of additional structures including planar polar (PP) and planar polar with two line defects (PPLD). In these latter configurations the director lies in a plane perpendicular to the axis of the cylinder with a strong component along a single in-plane direction (see Fig. 2.2). In the PP structure the local director is uniform near the axis of the cylinder and radial at the boundary. One can think about this configuration as if two half–integer disclination lines were pushed out of the cylinder leaving defectless structure inside the cylinder as shown at Fig. (2.2a). Crawford *et. al.* [4] obtained an analytical solution for the director configuration for PP, which is for weak anchoring W is:

$$\psi(r,\theta) = \frac{\pi}{2} - tan^{-1}\left\{\frac{R^2 + \gamma \cdot r^2}{R^2 - \gamma \cdot r^2}\ tan\theta\right\} \tag{2.3}$$

where the angle $\psi(r,\theta)$ is measured in the plane perpendicular to the axis with respect to radial direction and (r,θ) are usual polar coordinates. Here we define $\gamma = (\xi^2+1)^{1/2} - \xi$ and $\xi = 2K/RW$.

The free energy per unit length of the cylinder is given by:

$$F_{PP} = \pi K \Big\{ - ln(2\xi\gamma) + (1-\gamma)/\xi \Big\} \tag{2.4}$$

From these equations one can expect that ER structure should form for large dimensionless parameter RW/K avoiding costly deformation associated with the core. In the PPLD structure there are two half–integer disclination lines parallel to the cylinder axis and the distance between these lines is roughly temperature independent and approximately equals to the radius of the cylinder.

Kralj and Zumer [5] carried out a very complete numerical stability analysis of the various nematic structures in a cylindrical geometry by minimizing the Frank elastic energy (including the saddle–splay elastic constant K_{24}). For most values of the elastic constants they found a phase diagram with ER and PP structures, with the ER structure stable for large radii and/or strong anchoring. In particular if the bend and splay elastic constants are equal and $K_{24} = 0$, then the ER structure should form when RW/K exceeds about 27 [6], where R, W and K are the cylinder radius (measured in units of intermolecular spacing), surface anchoring strength, and Frank elastic constant respectively. However, a PR structure appears if the twist constant is very large compared with splay. They also found that the PPLD structure can be stabilized if K_{24} is nearly zero, R is approximately 100, and the half–integer defect lines are separated by a distance approximately equal to the diameter of the cylinder. An analytic study of these director structures was carried out by Burylov [7] with similar results.

Monte Carlo (MC) simulations of a cylindrically confined nematic with radial homeotropic boundary conditions were first performed by Chiccoli *et al.* [8] using the Lebwohl–Lasher lattice model [9]. This model represents each mesogenic molecule or small group of molecules by a three–dimensional spin vector. These spins are free to rotate about their centers which are fixed on the sites of a lattice. Spins whose distance r from the center of the cylinder is less than R, the radius of the cylinder, interact with their nearest–neighbors through the usual bulk Lebwohl–Lasher pair potential:

$$U_{ij} = -\epsilon_b P_2(\cos\theta_{ij}) \tag{2.5}$$

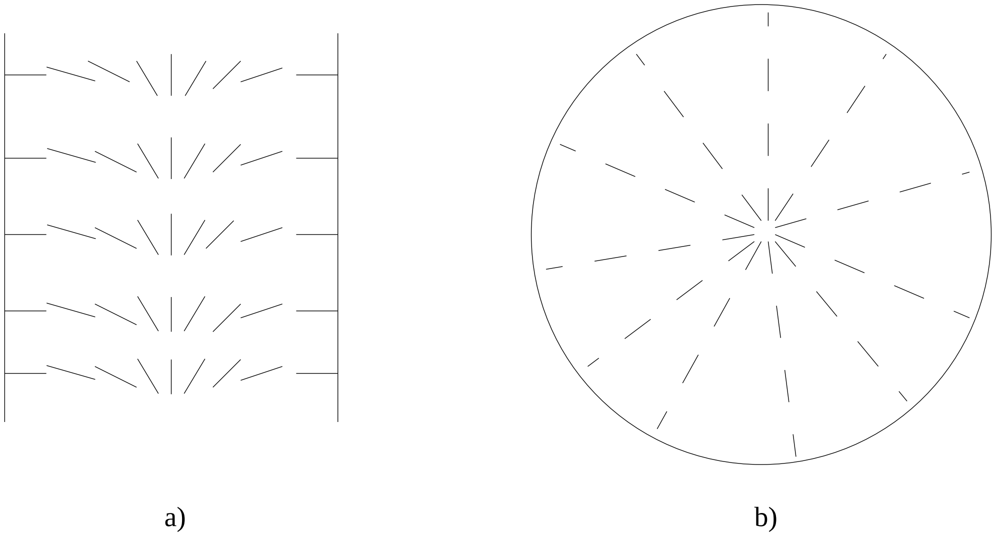
a) b)

Figure 2.1: Schematic director pattern in the (a) escaped radial (ER), and (b) planar radial (PR) configurations. The cylinder axis is vertical in (a) and perpendicular to the page in (b).

where θ_{ij} is the angle between two spins i and j, P_2 is a second rank Legendre polynomial and ϵ_b is a positive constant for nearest–neighbor sites and zero otherwise. The homeotropic surface anchoring is introduced via a group of boundary layer spins located at distances $R < r < R_c$ which point in a fixed radial direction. The interaction of these spins with the spins inside the cylinder is described by the potential:

$$U_{ik} = -\epsilon_s P_2(\cos\theta_{ik}) \tag{2.6}$$

where spin i is located inside the cylinder and spin k is the nearest–neighbor fixed spin which belongs to the boundary layer. The coupling ϵ_s is the surface anchoring strength. The total potential energy is given by the sum of the two energies above, summed over all pairs of spins. Note that in the Lebwohl-Lasher model, because the energy is invariant under a uniform rotation of all the spins, the bend, splay and twist elastic constants are equal, and the saddle splay elastic constant K_{24} is identically zero.

Chiccoli *et al.* [8] studied cylinders of radii 6 and 11 lattice spacings and heights $40, 52, 62$, and 82 lattice spacings with periodic boundary conditions along the cylinder axis. The spins were placed on the sites of a simple cubic lattice and the director structures were studied at a temperature of 0.6, measured in units of ϵ_b. Various values of the ratio of the surface anchoring strength ϵ_s to the

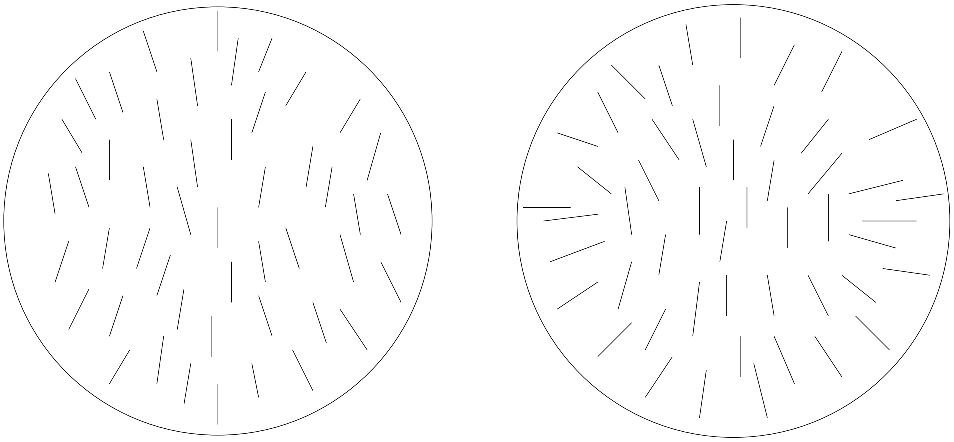

a) b)

Figure 2.2: Schematic director pattern in the (a) planar polar (PP), and (b) planar polar with line defects (PPLD) configurations. The cylinder axis is perpendicular to the page.

bulk nearest–neighbor coupling ϵ_b were considered, the largest being unity. In all cases, a planar structure was observed; however, these authors did not determine whether this structure is PP or PPLD.

Subsequently Smondyrev and Pelcovits [10] carried out Monte Carlo simulations on much larger Lebwohl–Lasher systems up to radii $R = 160$, with a height of 16, again using a simple cubic lattice. For low values of the radius or anchoring strength they found a PPLD structure, whereas for $RW/K = 160, \epsilon_s/\epsilon_b = 1$, and a temperature of 0.9, they obtained a metastable ER configuration. But this metastable structure eventually collapsed to a planar state, apparently in contradiction with elastic theory which [5] predicts that the ER structure should be stable when RW/K exceeds approximately 27. If we assume (incorrectly, as we show in Sec. 2.2) that the ratio ϵ_s/ϵ_b equals the corresponding Frank elastic energy ratio W/K, then Smondyrev and Pelcovits were simulating a system with $RW/K = 160$, far in excess of the critical value of 27.

Bradač *et al.* [11] carried out molecular dynamics simulations on cylindrically confined nematics interacting with a modified induced–dipole–induced–dipole interaction. For systems quenched from the isotropic phase to temperatures deep in the nematic phase, a phase diagram was obtained that is in reasonable agreement with the predictions of elastic theory. For the largest systems studied (radii of 16 lattice spacings) the PP, PPLD and ER structures were observed with increasing values of the surface interaction. For the case of equal elastic constants (i.e. like the Lebwohl–Lasher model) the ER structure appears when the ratio of the surface to bulk interaction energies is 0.2. However, these simulations were carried out for only 10000 time steps leaving open the possibility that the ER structure ultimately collapses. Also, these simulations were carried out at apparently lower temperatures than those used in the Monte Carlo simulations.

In this chapter we report the results of MC simulations of the confined Lebwohl–Lasher model which address the question of why the ER structure was not observed in previous MC simulations. We find that the ratio of the bulk–to–surface couplings in the Lebwohl–Lasher model, ϵ_b/ϵ_s, is *not* equal to K/W, except at very low temperatures. The latter quantity is equivalent [12] to the surface extrapolation length b. We find that there is significant dependence of b on temperature in the Lebwohl–Lasher model; in particular b grows as the NI transition temperature is approached from below (a feature observed in experimental studies of confined nematics [13, 14]). Thus, identifying the parameter $R\epsilon_s/\epsilon_b$ with $RW/K \equiv R/b$ is in general incorrect. Except at very low temperatures RW/K will be less than $R\epsilon_s/\epsilon_b$ (substantially so near the NI transition). Comparing the results of simulations with the predictions of elastic theory then requires consideration of this difference.

We also find, for large enough systems, that the rate at which the system is cooled from the isotropic to the nematic phase determines which director structure is ultimately observed in a simulation. Because b is large near the NI transition, a slow cooling rate will first yield a PPLD structure in this temperature range, in agreement with elastic theory which predicts that the PPLD is stable for small values of R/b. However, because of the large free energy barrier between the ER and PPLD structures, continued slow cooling to lower temperatures (where b is small and elastic theory predicts the appearance of the ER structure for sufficiently large R) will not yield the expected ER structure; the system becomes trapped in the metastable PPLD state. On the other hand, a relatively rapid cooling from the isotropic phase to low temperatures bypasses the PPLD state and allows the ER structure to form. To our knowledge, this is the first time a stable ER structure has been seen in a Monte Carlo simulation of confined nematics.

This chapter is organized as follows. In the Sec. 2.2 we describe our measurements of the surface extrapolation length and its temperature dependence. In Sec. 2.3 we report on simulations of a cylindrically confined nematic, exploring the effect of different cooling rates on the formation of the ER and PPLD structures. We offer some concluding remarks in the final section 2.4.

2.2 Surface Extrapolation Length

To measure the temperature dependence of the surface extrapolation length b, we consider a modification of the discussion presented in Ref. [12], where this length is defined by examining the director profile in a nematic confined between two plates which impose a twist distortion that is uniform across the sample except near the plates. The twist geometry is appropriate for studying planar anchoring at a surface. As we are interested in homeotropic alignment we consider instead a splay geometry. As shown in Ref. [12] the extrapolation length can be defined by extrapolating the constant slope portion of the director profile corresponding to the uniform twist or splay distortion; see Fig. (2.3). By minimizing the total elastic energy consisting of the bulk Frank energy in the one–elastic constant approximation and the surface energy, it was shown in Ref. [12] that the length b so defined is related to the Frank elastic constant K and the surface energy W by $b = K/W$.

We measured b defined in the above fashion in the Lebwohl–Lasher model on a cubic lattice of linear size 40. The spins on the plane $z = 39$ were coupled via the homeotropic surface interaction, Eq. (2.6) to the boundary spins on the plane $z = 40$ which are aligned along the z axis. Spins on the opposite wall, $z = 0$, were rigidly aligned parallel to the x axis. These spins interact with their interior neighbors via the bulk interaction, Eq. (2.5). Periodic boundary conditions were imposed on the remaining four sides of the lattice. In Fig. (2.3) we assume that the derivative of the angle $\theta(0)$ is constant in a bulk phase:

$$\frac{d\theta(z)}{dz} = \frac{\theta(L) - \theta(0)}{L} \tag{2.7}$$

On the other hand the surface prefers to have $\theta(0) = 0$. Therefore we have a competition between

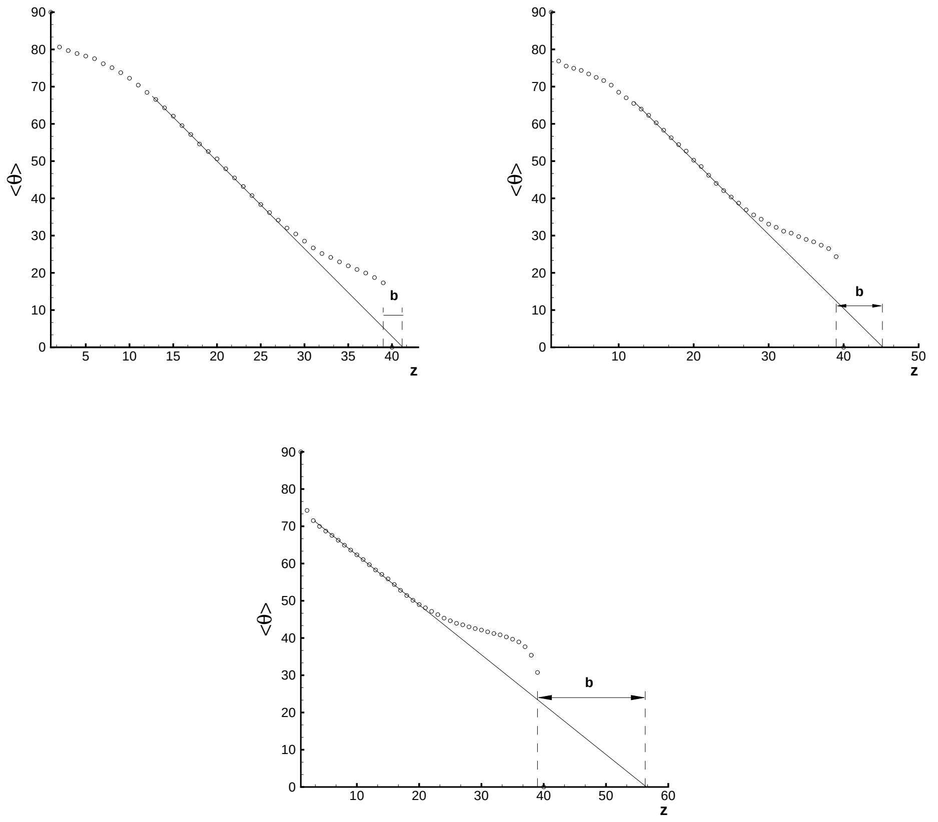

Figure 2.3: Measurement of the extrapolation length b in a Lebwohl–Lasher model of linear size 40 for three representative temperatures: a) $T = 0.5$, b) $T = 0.85$, and c) $T = 1.05$, (the NI transition is approximately 1.1). In each plot the average value (in degrees) of θ, the angle made by the spins with z axis is shown as a function of z, where z is measured in units of the lattice spacing. The spins at $z = 0$ are rigidly aligned parallel to the x axis, while the spins at $z = 39$ are coupled homeotropically with $\epsilon_s = 0.9$ to the spins at $z = 40$ which are aligned parallel to the z axis. Following [14] we define the extrapolation length b as shown in the figures. The solid straight lines are the best fits (to the eye) of the bulk splay distortion imposed by the boundary conditions. The numerical values of b for these three temperatures are 2.1, 6.2 and 17.3 respectively. Values for other temperatures and a smaller value of the surface coupling are given in Table 2.1.

Table 2.1: Temperature dependence of the extrapolation length b for two different values of the surface coupling ϵ_s. The bulk coupling ϵ_b is unity in both cases. The system is a cubic lattice of linear size 40.

T	$\epsilon_s = 0.45$	$\epsilon_s = 0.9$
1.0	11.3	10.5
0.9	8.5	7.1
0.8	7.0	5.0
0.7	5.1	4.1
0.6	3.0	2.8
0.5	2.1	2.1

surface and bulk terms in the total free energy:

$$F = \frac{1}{2} W \theta^2(0) + \frac{1}{2} K L \left(\frac{\theta(L) - \theta(0)}{L} \right)^2 \tag{2.8}$$

Minimizing the above equation with respect to $\theta(0)$ one can easily obtain the expression for the angle $\theta(0)$:

$$\theta(0) = \frac{K}{W} \frac{d\theta(z)}{dz} = \frac{1}{b(T)} \frac{d\theta(z)}{dz} \tag{2.9}$$

which is the definition of the extrapolation length $b = K/W$.

Starting in the isotropic phase the system was cooled down in temperature steps of 0.05. We equilibrated at least 200000 MC steps at each value of the temperature. We display results in Fig. (2.3) for three values of temperature ranging from deep in the nematic phase to near the NI transition. For each value of z we plot the average value of the spin's angle with the z axis (averaging over all sites in the $x-y$ plane). We determined b by extrapolating the linear director profile predicted by Frank elastic theory. Note that b is measured from $z = 39$, the layer of spins which are coupled homeotropically to the fixed boundary spins at $z = 40$. We note that b appears to diverge near the NI transition temperature in agreement with experimental results [13, 14]. Additional data for b as a function of T and ϵ_s is shown in Table 2.1. As expected, b increases with decreasing surface coupling.

Strong subsurface deformation is present as indicated by the deviation of the director profile

Table 2.2: Temperature dependence of R/b for cylinders of radii 80 and 120 with $\epsilon_s/\epsilon_b = 0.9$. The surface extrapolation length b is given in Table 2.1. According to elastic theory the PPLD structure should be stable for R/b less than approximately 27, while the ER structure should be stable for larger values of R/b.

T	$R/b, R = 80$	$R/b, R = 120$
1.0	7.6	11.4
0.9	11.3	16.9
0.8	16.0	24.0
0.7	19.5	29.3
0.6	28.6	42.9
0.5	38.1	57.1

from the linear behavior predicted by Frank elastic theory. It is not clear to us what the origin of this deformation is. Previous work on subsurface deformations [15] found that the deformation arises for anisotropic interactions which is not the case for the Lebwohl–Lasher model. However, our determination of the extrapolation length b is not affected by the subsurface deformation.

It is worth commenting on the value of b that would be obtained by examining the director pattern near the strongly anchored wall, $z = 0$. The spins on this wall are coupled via the bulk interaction (with a coupling ϵ_b of unity) to the spins on the plane $z = 1$. Thus, one can think of these latter spins as having a *homotropic* surface interaction with the surface at $z = 0$. Extrapolating the director profile to negative z and measuring b from $z = 1$ would yield a value of b comparable to that obtained at the opposite wall, $z = 40$. Note, however, that because the effective surface coupling ϵ_s is unity on the $z = 0$ wall, the value of b extracted there will be somewhat smaller than that obtained on the opposite wall where we used $\epsilon_s = 0.9$.

The strong dependence of b on temperature indicates that W, the surface energy, has a different dependence on temperature than the Frank elastic constant K. The latter was measured in the Lebwohl–Lasher model by Cleaver and Allen [16], who found it to be approximately proportional to S^2, where S is the nematic order parameter. Experimental measurements of b [13] find that it diverges as $(T_{NI} - T)^{-1}$, where T_{NI} is the NI transition temperature, which suggests that W is proportional to S^4. Our data is not sufficiently robust to determine the dependence of W on S.

The temperature dependence of b helps to explain the apparent discrepancy between the results of previous simulations [8, 10] and elastic theory [4], summarized in Sec. 2.1. Even at a relatively low temperature $T = 0.6$ as was used in Ref. [8], b is of order 3, and thus the elastic theory parameter $RW/K = R/b$ that determines the relative stability of the various director structures is approximately one–third the value of the corresponding Lebwohl–Lasher "bare" parameter, $R\epsilon_s/\epsilon_b$. Ref. [10] reported on simulations carried out at $T = 0.9$ with $\epsilon_s/\epsilon_b = 1.0$, where the Lebwohl–Lasher parameter is approximately 7 times greater than RW/K. Thus the simulations carried out in this latter work at a value of $R = 160$, in reality correspond to $RW/K \approx 23$, i.e., below the threshold value for the formation of the ER structure. On the other hand, the simulations of Ref. [11] were carried out deep in the nematic phase where RW/K and $R\epsilon_s/\epsilon_b$ should be nearly equal.

2.3 Stability of the ER and PPLD structures

With the insight gained in the previous section regarding the proper comparison of simulation results with elastic theory, we carried out additional MC simulations on the Lebwohl–Lasher model confined to a cylinder. Previous simulation studies of nematics confined to cylinders [8, 10, 11] were done on a cubic lattice. However, this choice of lattice biases the position of the two disclination lines in the PPLD structure; in particular they always appear on one of the two crystalline axes perpendicular to the long axis of the cylinder. In addition approximately half of the spins on the perimeter of the cylinder have *two* nearest–neighbor spins on the fixed boundary layer (see Eq. 2.6), whereas the other half have only one such nearest–neighbor, resulting in a nonuniform coupling of the nematic to the cylindrical surface.

To eliminate this nonuniformity we worked instead with a honeycomb lattice. With this choice nearly all spins on the perimeter of the cylinder have only one nearest–neighbor in the boundary layer. While the honeycomb lattice does not have continuous rotational symmetry about the cylinder axis, we found that its higher symmetry about this axis (six–fold as compared to four–fold for the cubic lattice) led to the appearance of the disclination lines in the PPLD structure on axes not necessarily along the crystal lattice directions. The honeycomb lattice is bipartite allowing us to implement a standard "checkerboard" algorithm [17], an efficient choice for vector processors. We divided the system into two interconnected sublattices and then alternately updated spins on each.

As in Ref. [10] we determined the nature of the resulting director structures by computing an escaped order parameter, which measures the degree of spin tilt away from the plane perpendicular to the cylinder axis, and is a sensitive measure of the presence of the ER structure. It is given by:

$$P_2^{esc} = \frac{1}{N}\sum P_2(\hat{\mathbf{u}}_\mathbf{i} \cdot \hat{\mathbf{z}}) \tag{2.10}$$

where the cylinder axis is along the z direction. The escaped order parameter is calculated as a function of the distance from the center of the cylinder, and the sum is over spins in a thin annulus with the same height as the cylinder.

We explored the stability of the PPLD and ER structures for systems of two different radii, 80 and 120, both of height 16, with $\epsilon_s/\epsilon_b = 0.9$. In Table 2.2 we tabulate the values of R/b for these two radii using the data for b from Table 2.1. Using the table we see that elastic theory predicts that the PPLD structure should be stable for temperatures greater than approximately 0.6 and 0.7, for $R = 80$ and 120, respectively, while the ER structure should be stable at temperatures below these values. Note that elastic theory by its nature is unable to predict the transition temperature separating the PPLD and ER structures from the isotropic phase. Beginning in the isotropic phase at $T = 1.4$ we cooled the system of $R = 80$, in temperature steps of 0.1 equilibrating 100000 MC steps at each temperature. At $T = 0.9$ a stable PPLD structure was formed. We checked the stability of this structure up to 500000 MC steps. Upon further cooling down to $T = 0.5$ (again equilibrating 100000 MC steps at each temperature) the system remained trapped in the PPLD structure even though at this lower temperature $b = 2.1$ and $R/b = 38.1$, well above the threshold predicted by elastic theory for the formation of the ER structure. We found similar behavior irrespective of the cooling rate used, including instantaneous quenches directly from the isotropic phase. Conversely, if we began at $T = 0.8$ with an ER configuration constructed by hand using the mathematical form derived in Refs. [2, 3], we found this state to be stable even after 500000 MC steps. Yet for this value of T the PPLD state should be stable ($R/b = 16.0$). These results suggest that there is a large free energy barrier separating the PPLD and ER structures, and the system can be trapped in either state.

We found somewhat different results for the larger radius system, $R = 120$. We cooled this system down from $T = 1.4$ again in temperature steps of 0.1 equilibrating 300000 MC steps at each value of temperature. As expected a stable (up to 500000 MC steps) PPLD structure was formed at $T = 0.9$ ($R/b = 16.9 < 27$). Upon further cooling the system remained trapped in the PPLD state, just as in the case of the smaller system. However, if the same system were equilibrated 100000 MC steps at each temperature step as it was cooled from $T = 1.4$ to $T = 0.8$, then an ER structure was formed at the latter temperature and remained stable up to 500000 MC steps. In this case the more rapid rate of cooling allowed us to bypass the incipient PPLD structure at $T = 0.9$ and reach a stable ER structure. At $T = 0.8$, $b = 5$, and $R/b = 24$, which is slightly below the critical value of 27 predicted by elastic theory. We suspect that our ability to form an ER structure for this system of larger radius is due to the smaller temperature range (0.9 to 0.75) where the PPLD structure is stable compared with the case of $R = 80$, where the PPLD structure, according to elastic theory and Table 2.2, should be stable from $T \simeq 0.9$ down to $T \simeq 0.6$.

2.4 Summary of the Results

In this chapter we have addressed the question of reconciling the predictions of elastic theory with the results of numerical simulations for nematics confined to cylindrical cavities with homeotropic boundary conditions. Our main result is that care must be taken in comparing elastic theory with numerical simulations because of the strong temperature dependence of the ratio K/W, the surface extrapolation length. Except at very low temperatures, this ratio is much *larger* than the corresponding “bare” ratio of bulk and surface energies in a numerically simulated model. When this difference is taken into account, the results of numerical simulations are consistent with the predictions of elastic theory. In particular, the ER structure forms for values of RW/K above the critical value of 27 predicted by elastic theory, providing that the metastable PPLD structure can be avoided. Because K/W is very large near the NI transition, and thus RW/K is relatively small, the system will readily form a PPLD structure if it is cooled slowly from the isotropic phase. However, with rapid cooling and for large enough systems where the PPLD phase is limited in its temperature range, this state can be bypassed and a stable ER structure formed at lower temperatures where RW/K is sufficiently large.

Bibliography

[1] *Liquid crystals in complex geometries*, edited by G. P. Crawford and S. Zumer, (Taylor & Francis, London, 1996).

[2] P. E. Cladis and M. Kleman, J. Phys.(Paris), **33**, 591 (1972).

[3] R. B. Meyer, Phil. Mag. **27**, 405 (1973).

[4] D. W. Allender, G. P. Crawford, and J. W. Doane, Phys. Rev. Lett. **67,** 1442 (1991);
G. P. Crawford, D. W. Allender, and J. W. Doane, Phys. Rev. A **45,** 8693 (1992);
S. Kralj and S. Žumer, Phys. Rev. A **45,** 2461 (1992);
S. Kralj and S. Žumer, Liq. Cryst. **15,** 521 (1993).

[5] S. Kralj and S. Žumer, Phys. Rev. E **51,** 366 (1995).

[6] In the one constant approximation this critical value of RW/K separating the ER and PP structures can also be obtained analytically; see Ref. [4].

[7] S. V. Burylov, Sov. Phys. JETP **85,** 873 (1997).

[8] C. Chiccoli, P. Pasini, F. Semeria, E. Berggren, and C. Zannoni, Mol. Cryst. Liq. Cryst., **290**, 237 (1996).

[9] P. A. Lebwohl and G. Lasher, Phys. Rev. A **47**, 4780 (1972).

[10] A. M. Smondyrev and R. A. Pelcovits, Liq. Cryst. **26**, 235 (1999).

[11] Z. Bradač, S. Kralj, and S. Žumer, Phys. Rev. E **58**, 7447 (1998).

[12] P. de Gennes and J. Prost, *The Physics of Liquid Crystals* (Clarendon Press, Oxford, 1993).

[13] A. Mertelj and M. Čopič, Phys. Rev. Lett. **81**, 5944 (1998).

[14] D.-S. Seo, Y. Limura, and S. Kobayashi, Appl. Phys. Lett. **61**, 234 (1992); T. Sugiyama, S. Kuniyasu, and S. Kobayashi, Mol. Cryst. Liq. Cryst. **238**, 1 (1994).

[15] G. Barbero, L. R. Evangelista, and S. Ponti, Phys. Rev. E **53**, 1265 (1996); G. Skačej, V. M. Pergamenshchik, A. L. Alexe-Ionescu, G. Barbero, and S. Žumer, Phys. Rev. E **56**, 571 (1997); G. Skačej, A. L. Alexe-Ionescu, G. Barbero, and S. Žumer, Phys. Rev. E **57**, 1780 (1998);

[16] D. J. Cleaver and M. P. Allen, Phys. Rev. A **43**, 1918 (1991)

[17] D. P. Landau, in *The Monte Carlo Method in Condensed Matter Physics*, edited by K. Binder, (Springer, Berlin, 1995), second edition.

Chapter 3

Simulations of the Nematic–Isotropic Transition

In this chapter we report the results of simulations of the three–dimensional Lebwohl–Lasher model of the nematic–isotropic transition using a single cluster Monte Carlo algorithm. The algorithm, first introduced by Kunz and Zumbach to study two–dimensional nematics, is a modification of the Wolff algorithm for spin systems, and greatly reduces critical slowing down. We calculate the free energy in the neighborhood of the transition for systems up to linear size 70. We find a double well structure with a barrier that grows with increasing system size. We thus obtain an upper estimate of the value of the transition temperature in the thermodynamic limit.

The Lebwohl–Lasher (LL) model [1] is a lattice model of rotors with an orientational order–disorder transition. While it neglects the coupling between the orientational and translational degrees of freedom present in a real nematic liquid crystal, it is generally believed that this coupling does not play a significant role at the nematic–isotropic (NI) transition. With the absence of translational degrees of freedom the LL model is particularly well–suited for large–scale simulations of the transition. The model is defined by the Hamiltonian:

$$\mathcal{H} = -\epsilon \sum_{<ij>} \left\{ \frac{3}{2}(\hat{\sigma}_i \cdot \hat{\sigma}_j)^2 - \frac{1}{2} \right\} \tag{3.1}$$

where the sum is over all nearest-neighbors and ϵ is a coupling parameter. The long axes of the rotors are specified by unit vectors $\hat{\sigma}_i$. The LL model has been intensively investigated using Monte Carlo techniques since its introduction [2, 3, 4, 5, 6, 7].

As in real experimental systems the NI transition in the LL model is weakly first–order; thus, there is significant critical slowing down in the neighborhood of the transition. In a Monte Carlo simulation the system gets trapped in one of the free energy wells corresponding to the nematic or isotropic phase, and the conventional single flip Metropolis algorithm becomes inefficient especially as the system size is increased. While Boschi *et al.* [7] carried out simulations on systems as large as $120 \times 120 \times 120$, the most detailed study of the NI transition was carried out by Zhang *et al.* [6] on systems up to $28 \times 28 \times 28$. These authors used the Lee–Kosterlitz finite size scaling method [8, 9], supplemented by the Ferrenberg–Swendsen reweighting technique [10] to determine the order of the NI transitions and estimate the value of the transition temperature T_c in the thermodynamic limit. In the Lee–Kosterlitz method one examines the finite size scaling of the free energy barrier ΔF between the nematic and isotropic phases; at a first–order transition this should be an increasing function the linear system size L, while it should approach a constant for systems with continuous phase transitions. For a large enough system, specifically $L \gg \xi$, where ξ is the correlation length, a finite size scaling analysis predicts that $\Delta F \sim L^2$ for three–dimensional systems. In the LL model Zhang *et al.* found a small free energy barrier appearing at the two largest system sizes they studied, $L = 24$ and 28, and thus did not have enough data to carry out a finite size scaling analysis of ΔF. Instead they estimated the value of T_c in the thermodynamic limit by extrapolating three different measures of T_c: the positions of the maxima in the specific heat and susceptibility and the the temperature where the two free energy wells are of equal depth. However, as we demonstrate below, the system sizes considered by Zhang *et al.* are not in the finite–size scaling regime, and thus their estimate of T_c in the thermodynamic limit is not accurate.

3.1 Single Cluster Monte Carlo Algorithm

Over the past decade significant advances have been made in algorithm development which overcome critical slowing down in magnetic spin systems [11]. In particular single cluster algorithms have proven to be very efficient in simulating the three–dimensional Ising, XY and Heisenberg models. These algorithms are nonlocal updating methods where a single cluster of spins is constructed and the spins within the cluster are updated simultaneously. In the Ising case [12] clusters of spins are formed by creating bonds between parallel spins with a probability that guarantees detailed balance. For models with continuous symmetry Wolff [13] introduced a cluster algorithm where "parallel spins" refer to spins which point in the same hemisphere. A hemisphere is defined by an equatorial plane perpendicular to a randomly chosen direction $\hat{\mathbf{r}}$. Nematic liquid crystals differ in an important symmetry aspect from magnetic systems, namely, "up" and "down" spins are equivalent. To construct a cluster algorithm suitable for simulating the LL model the Wolff algorithm must be modified to account for this symmetry difference. The necessary modification was done by Kunz and Zumbach [14], and used by them to study the two–dimensional LL model. Here we use their algorithm, along with the Lee–Kosterlitz finite size scaling method, to study the first–order transition in the three–dimensional LL model.

Following Kunz and Zumbach, we randomly choose a direction $\hat{\mathbf{r}}$. Then we reflect any molecular long axes for which $\hat{\sigma}_i \cdot \hat{\mathbf{r}} < 0$, by the transformation $\hat{\sigma} \to -\hat{\sigma}$; note that the Hamiltonian $\mathcal{H}$ is invariant under this operation. Next we choose a site i at random and reflect it, $\hat{\sigma}_i' = R(\hat{\mathbf{r}})\hat{\sigma}_i$ using the reflection operator $R(\hat{\mathbf{r}})$ defined by:

$$R(\hat{\mathbf{r}})\hat{\sigma}_i = -\hat{\sigma}_i + 2(\hat{\sigma}_i \cdot \hat{\mathbf{r}})\hat{\mathbf{r}}. \tag{3.2}$$

This operation is illustrated in Fig. (3.1a). Unlike the original Wolff reflection operation which reflects spins from the original hemisphere to the opposite one, the present reflection operator keeps the molecular orientation vectors in the same hemisphere defined by $\hat{\mathbf{r}}$. Next we form bonds with the nearest–neighbors of $\hat{\sigma}_i'$ with probability:

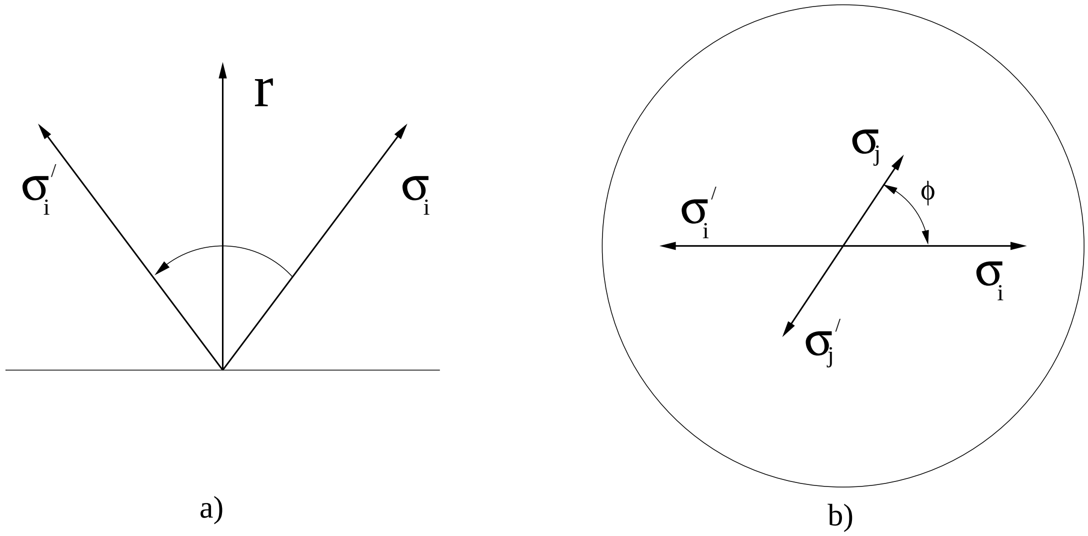

Figure 3.1: (a) Illustration of the reflection operation $R(\hat{\mathbf{r}})$, Eq. (3.2). The unit vector $\hat{\mathbf{r}}$ is chosen randomly at the start of the algorithm. The reflection operation yields the new molecular orientation $\sigma_i' = R(\hat{\mathbf{r}})\sigma_i$ as shown. (b) Illustration of the formation of a cluster of two molecules. Here we show the projections of the two molecular long axes σ_i and σ_j on the plane perpendicular to $\hat{\mathbf{r}}$, as well as the projections of the molecular long axes produced by the reflection operator $R(\hat{\mathbf{r}})$ acting on these two molecules. Two molecules are likely to form a cluster if they each make an angle of approximately 45° with $\hat{\mathbf{r}}$ and if the angle ϕ between their projections is less than 90°.

$$\begin{aligned} P_{ij} &= 1 - \exp\left\{ \min\left[0, \beta(\hat{\sigma}_i' \cdot \hat{\sigma}_j)^2 - \beta(\hat{\sigma}_i' \cdot (R(\hat{\mathbf{r}})\hat{\sigma}_j))^2\right]\right\} \\ &= 1 - \exp\left\{ \min\left[0, 4\beta(\hat{\sigma}_i' \cdot \hat{\mathbf{r}})(\hat{\sigma}_j \cdot \hat{\mathbf{r}})\Big((\hat{\sigma}_i' \cdot \hat{\sigma}_j) - (\hat{\sigma}_i' \cdot \hat{\mathbf{r}})(\hat{\sigma}_j \cdot \hat{\mathbf{r}})\Big)\right]\right\}, \qquad (3.3) \end{aligned}$$

where $\beta = 3\epsilon/2k_BT$. This probability is a modification of the one introduced by Wolff, replacing the Heisenberg interaction $-J\hat{\sigma}_i \cdot \hat{\sigma}_j$ by the Lebwohl–Lasher interaction $-\frac{3}{2}\epsilon(\hat{\sigma}_i \cdot \hat{\sigma}_j)^2$. As in the original Wolff algorithm we continue this process, forming bonds with the nearest–neighbors of all reflected molecular orientation vectors until the cluster cannot grow any further.

To understand the formation of clusters, consider the projection of two molecular orientation vectors, $\hat{\sigma}_i$ and one of its nearest–neighbors $\hat{\sigma}_j$, on the plane perpendicular to $\hat{\mathbf{r}}$ before the reflection operation is performed (see Fig. 3.1b). A bond between these two molecules will likely form if the angle ϕ between their projections is less than 90°. Note that the probability Eq. (3.3) for the bond formation is maximized when the angle between $\hat{\sigma}_i'$ and $\hat{\sigma}_j$ is 90° and each of these molecules makes an angle of 45° with $\hat{\mathbf{r}}$. Thus, as in the original Wolff algorithm at low temperatures the molecules are nearly all aligned and it is highly probable that a large fraction of all molecules will be flipped at once. On the other hand at high temperatures the distribution of molecules will be isotropic, resulting in flipping small clusters in random directions. In the intermediate region close to the NI transition temperature the system flips between isotropic and nematic states.

3.2 Theory of Finite Size Scaling

We have used the cluster algorithm to simulate the LL model on a simple cubic lattice of linear dimension L, $30 \leq L \leq 70$, with periodic boundary conditions, in order to study the properties of the NI transition. The temperature T was measured in dimensionless units of ϵ/k_B, in agreement with the units used in previous studies of this model. Our initial random configurations were equilibrated at least 200000 Monte Carlo steps (MCS) before starting production runs. We found that the average cluster size at temperatures close to the NI transition is approximately $0.17N$ sites per cluster (where N is the total number of lattice sites), essentially independent of system size. Approximately half of the MCS resulted in clusters with fewer than ten sites and were efficiently simulated with scalar code. However, a significant fraction of clusters had $N/2$ sites or greater, and employing a vectorizable cluster construction method [15] yielded a sixfold speedup.

For each configuration generated, we calculated the energy per site, $E = \mathcal{H}/N$. To ascertain the nature of the phase transition we proceeded as in Ref. [6] and used the method of Lee and Kosterlitz [8, 9], which relies on the single histogram reweighting technique of Ferrenberg and Swendsen [10]. Following the approach of the latter authors we stored the configuration data in a histogram $H(E,T,L)$. The normalized probability distribution function $P(E,T,L)$ of the energy is then given by:

$$P(E,T,L) = \frac{H(E,T,L)}{\sum_E H(E,T,L)} \tag{3.4}$$

Given this distribution function at temperature T, the Ferrenberg–Swendsen method allows the calculation of thermodynamic quantities at a different temperature T' in the neighborhood of T. Specifically, thermodynamic quantities at T' can be calculated using the distribution function $P(E, T', L)$ where:

$$P(E, T', L) = \frac{H(E, T, L)\exp(-\Delta\beta E)}{\sum_E H(E, T, L)\exp(-\Delta\beta E)} \tag{3.5}$$

and $\Delta\beta$ is the inverse temperature difference:

$$\Delta\beta = (\frac{1}{T'} - \frac{1}{T}). \tag{3.6}$$

Thus, accurate information over the entire critical region can be extracted from a small number of simulations.

The Lee–Kosterlitz method utilizes the system size dependence of the barrier ΔF separating the isotropic and nematic free energy minima at the transition temperature to determine the order of the transition. If the barrier grows with increasing the system size L then the transition is first order; furthermore, if finite size scaling holds, then $\Delta F \sim L^2$ in a three–dimensional system. Here L^2 dependence can be understood as a surface that separates ordered and disordered phases at coexistence in the first order phase transition.

To determine the barrier height we use the free–energy–like quantity:

$$F(E, T, L) \sim -\ln P(E, T, L) \tag{3.7}$$

which differs from the true free energy by additive quantities dependent only on T and L which are irrelevant to computations of free energy differences. The additive quantities simply mean that we performed a finite time simulations and our histogram $P(E, T, L)$ is nearly proportional to the exact one. This free–energy–like quantity is shown in Fig. (3.2) for different system sizes, and we note the appearance of a pronounced double–well structure for sufficiently large system sizes. The right and left hand wells correspond to the nematic and isotropic phases respectively. In collecting our data we made sure that system made at least 100 hops between the two wells for the largest

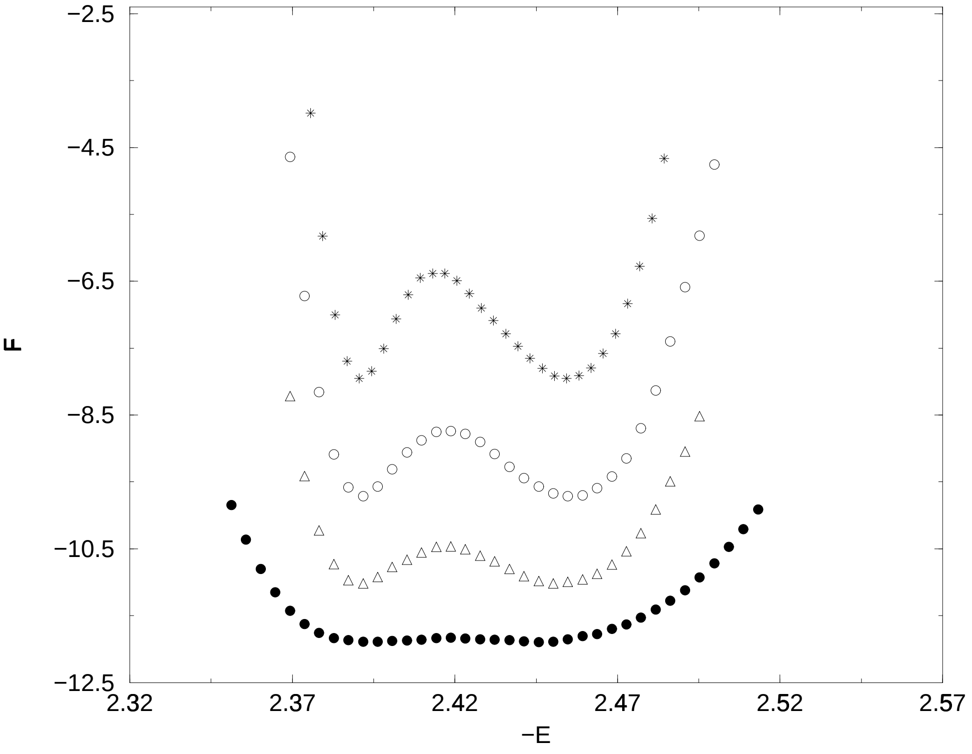

Figure 3.2: Free energy, Eq. (3.7), in units of ϵ as a function of the energy per unit site E (also measured in units of ϵ), for four different lattice sizes, $L = 30\ (\bullet), 50\ (\triangle), 60\ (\circ), 70\ (*)$. The data for the three largest system sizes have been displaced vertically for the sake of clarity.

system size of 70, for a run of 6×10^6 MCS. For each system size, we performed sufficient MCS such that the typical number of points in one bin of the histogram H is much larger than the variation in the exponential factor $\exp(\Delta T L^3)$, where $\Delta T = T' - T$. This criterion arises from the requirement that the peak in the reweighted distribution Eq. (3.5) avoid the "wings" of the measured histogram. Typically we found approximately 10^4 points in each bin and the exponential factor varied by about 10.

3.3 Free Energy Barrier and Critical Temperature

Zhang *et al.* [6] made similar plots of the free energy $F(S, T, L)$ as a function of the nematic order parameter S rather than the energy E. For the system sizes studied by these authors, with $L \leq 28$, the free energy function $F(E, T, L)$ is a much weaker indicator of the nature of the NI transition. However, for the system sizes we have studied, with $30 \leq L \leq 70$, the free energy as a function of E is a very good indicator as illustrated in Fig. (3.2). We calculated $F(S, T, L)$ for $L = 28$, the largest system size studied by Zhang *et al.* to check that our cluster algorithm yields the same transition temperature they determined using the conventional single spin flip MC algorithm. In general we did not calculate $F(S, T, L)$ because this requires calculation of a histogram $H(E, S, T, L)$, dependent on S as well as E in order to carry out the reweighting. Calculation of this multiple histogram with sufficiently good statistics is prohibitively time consuming for large systems.

The barrier height $\Delta F(L)$ can be computed as follows:

$$\Delta F(L) = F(E_m, T, L) - F(E_1, T, L) \tag{3.8}$$

where E_m is the energy corresponding to the top of the free energy barrier and E_1 is either one of the degenerate local minima. In the finite size scaling regime we would expect that $\Delta F \sim L^2$. Our results for the barrier height as a function of system size are shown in Fig. (3.3), where we plot $\Delta F/L^2$ versus L. It is apparent from our plot that even systems with $L = 70$ are not yet in the finite size scaling regime. We have estimated the system sizes needed to observe finite size scaling

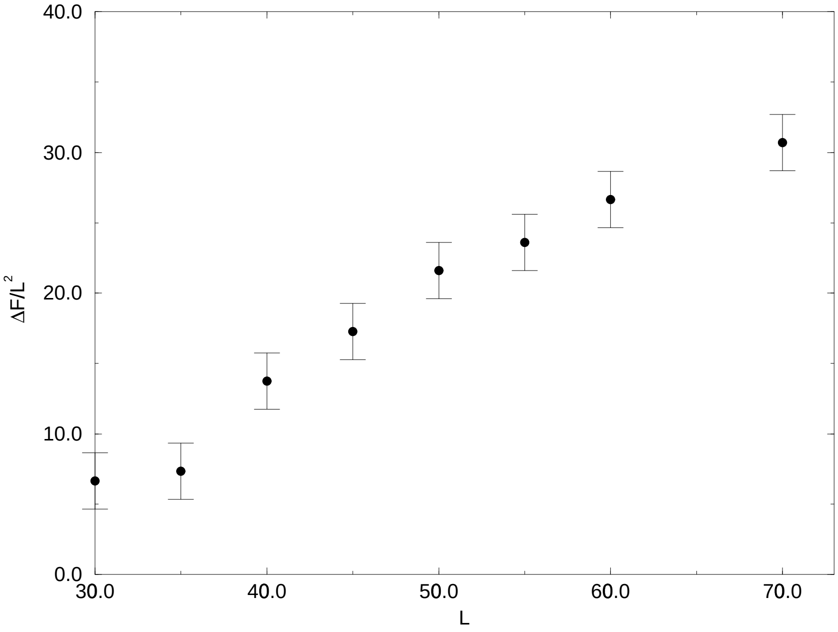

Figure 3.3: The free energy barrier height $\Delta F/L^2$ (measured in units of $10^{-5}\epsilon$ divided by the lattice spacing squared) as a function of L (measured in units of the lattice spacing). If finite size scaling were obeyed, $\Delta F/L^2$ would be independent of L.

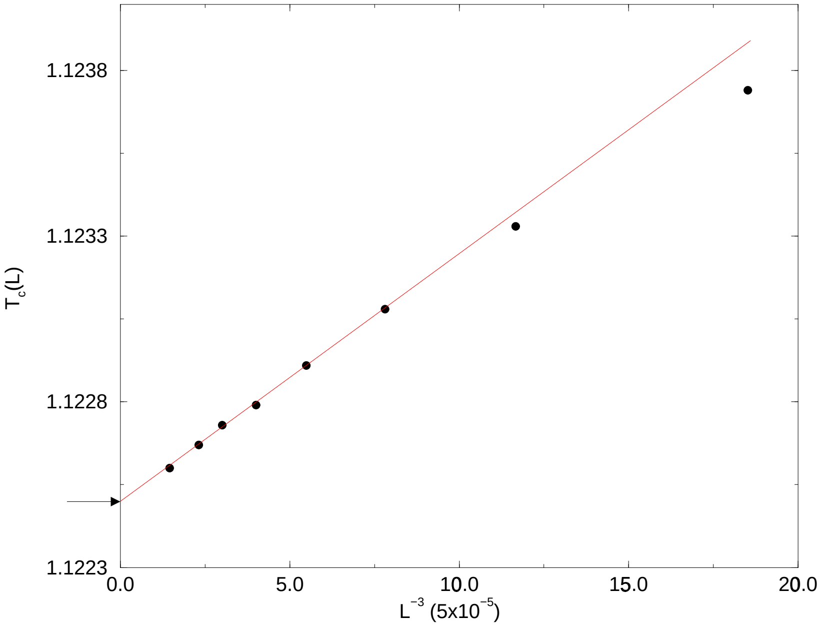

Figure 3.4: The transition temperature $T_c(L)$, (measured in units of ϵ/k_B) as a function of L^{-3} (in units of 5×10^{-5} inverse cubic lattice spacings), for the eight system sizes shown in Fig. (3.3), showing apparent finite size scaling behavior (the straight line fit) given by Eq. (3.9) for system sizes $L \geq 35$ (compare, however, with the behavior of the free energy barrier shown in Fig. (3.3). The extrapolation of this line to infinite system size yields an estimate for the upper bound on the transition temperature (indicated by the arrow) in the thermodynamic limit. The value of critical temperature is $T_c = 1.1225 \pm 0.0001$.

by fitting our data for $\Delta F(L)$ to the form $\Delta F(L) = aL^2 + bL + c$, where the term proportional to a is the finite size scaling law and the term proportional to b represents the leading correction to scaling. We find that the ratio $b/a \simeq 30$. Thus, to observe finite size scaling, one must have $L \gg 30$.

The transition temperature $T_c(L)$ for a particular system size L is given by the value of the temperature where the two free energy wells have equal depths. Our results for $T_c(L)$ are shown in Fig. (3.4). From the straight line plotted in the figure we see that the finite size scaling relation,

$$\Delta T = T_c - T_c(L) \simeq L^{-3}. \tag{3.9}$$

appears to work well for systems of size $L \gg 35$. Given the behavior of $\Delta F(L)$ shown in Fig. (3.3), one should view this relation with caution. However, we can use this relation to provide an estimate for an upper bound for the transition temperature from the intersection of the straight line with the $T_c(L)$ axis yielding $T_c = 1.1225 \pm 0.0001$. This value is lower than that obtained in Ref. [6], ($T_c = 1.1232 \pm 0.0001$), which is not surprising given that smaller system sizes were studied in the latter work.

3.4 Conclusions

In conclusion, we have used a modification of the single cluster Wolff algorithm for nematic systems to efficiently study the NI transition in Lebwohl–Lasher systems [16]. As in the case of the cluster algorithms developed originally for ferromagnetic models, this algorithm allows us to overcome the critical slowing down associated with conventional single–flip Monte Carlo. The phase space can then be sampled efficiently near the transition as the system will flip readily between the ordered and disordered phases. We have been able to observe for the first time a clear free energy barrier separating the nematic and isotropic phases, and have found that very large system sizes ($L \gg 30$) will be needed to observe finite size scaling behavior. We have also applied the algorithm to study the behavior of disclination loops in the transition region [17] and the efficiency of the algorithm allow the study of many other interesting properties of the transition, which we discuss in the next

Chapter.

Bibliography

[1] P. A. Lebwohl and G. Lasher, Phys. Rev. A **6**, 426 (1972).

[2] G. R. Luckhurst and P. Simpson, Mol. Phys. **47**, 251 (1982).

[3] U. Fabbri and C. Zannoni, Mol. Phys. **4**, 763 (1986).

[4] F. Biscarini, C. Zannoni, C. Chiccoli, and P. Pasini, Mol. Phys. **73**, 439 (1991).

[5] C. Zannoni, J. Chem. Phys. **84**, 424 (1986).

[6] Z. Zhang, O. G. Mouritsen, and M. J. Zuckermann, Phys. Rev. Lett. **69**, 1803 (1992); Z. Zhang, M. J. Zuckermann, and O. G. Mouritsen, Mol. Phys. **80**, 1195 (1993).

[7] S. Boschi, M. P. Brunelli, C. Zannoni, C. Chiccoli, and P. Pasini, Int. J. Mod. Phys. C **8** 547 (1997).

[8] J. Lee and J. M. Kosterlitz, Phys. Rev. Lett. **65**, 137 (1990).

[9] J. Lee and J. M. Kosterlitz, Phys. Rev. B **43**, 3265 (1991).

[10] A. M. Ferrenberg and R. H. Swendsen, Phys. Rev. Lett. **61**, 2635 (1988).

[11] For a review, see R. H. Swendsen, J. -S. Wang, and A. M. Ferrenberg, in *The Monte Carlo Method in Condensed Matter Physics,* second edition, edited by K. Binder (Springer, Berlin, 1995), pp. 75–91.

[12] R. H. Swendsen and J. S. Wang, Phys. Rev. Lett. **58**, 86 (1987).

[13] U. Wolff, Phys. Rev. Lett. **62**, 361 (1989)

[14] H. Kunz and G. Zumbach, Phys. Lett. B **257**, 299 (1991); Phys. Rev. B **46**, 662 (1992). See also, S. Caracciolo, R. G. Edwards, A. Pelissetto and A. D. Sokal, Nuc. Phys. B **403**, 475 (1993).

[15] H. G. Evertz, J. Stat. Phys. **70**, 1075 (1993).

[16] N. V. Priezjev and R. A. Pelcovits, Phys. Rev. E **63**, 062702 (2001).

[17] N. V. Priezjev and R. A. Pelcovits, Phys. Rev. E **64**, 031710 (2001).

Chapter 4

Disclination Loop Critical Behavior near the NI transition

We investigate the behavior of disclination loops in the vicinity of the first order nematic–isotropic transition in the Lebwohl–Lasher and related models. We find that two independent measures of the transition temperature, the free energy and the distribution of disclination line segments, give essentially identical values. We also calculate the distribution function $D(p)$ of disclination loops of perimeter p and fit it to a quasiexponential form. Below the transition, $D(p)$ falls off exponentially, while in the neighborhood of the transition it decays with a power law exponent approximately equal to 2.5, consistent with a “blowout” of loops at the transition. In a modified Lebwohl–Lasher model with a strongly first–order transition we are able to measure a jump in the disclination line tension at the transition, which is too small to be measured in the Lebwohl–Lasher model. We also measure the monopole charge of the disclination loops and find that in both the original and modified Lebwohl–Lasher models, there are large loops which carry monopole charge, while smaller isolated loops do not. Overall the nature of the topological defects in both models is very similar.

4.1 Role of the topological defects at the phase transitions

In many physical systems, particularly two–dimensional with continuous order parameter symmetry, topological defects can play an essential role at the phase transition between the ordered (or quasi–ordered) and disordered phases. Using simple physical arguments Kosterlitz and Thouless [1] pointed out that phase transitions in two–dimensional superfluid ^{4}He, crystalline solids and XY magnets would occur via the unbinding of point topological defects. Subsequently, Kosterlitz [2] developed a renormalization group theory for the two–dimensional XY model which provided quantitative predictions for this defect–mediated critical behavior. Renormalization group theories for the defect–mediated melting of crystalline solids in two–dimensions were developed by Nelson and Halperin [3] and Young [4].

The theoretical picture for defect–mediated phase transitions in three dimensions is less clear. It is expected on the basis of the Villain representation [5] that the transition in the three–dimensional XY model is mediated by vortex loops [6]. In this scenario there is a finite length scale at low temperatures associated with the typical size of vortex loops which disorder the system on smaller length scales. At the phase transition, loops can exist on all length scales, i.e. there is “vortex–loop blowout” [7, 8] and the system enters the disordered phase. Scaling and renormalization group theories have been developed [9] which provide quantitative predictions for the critical behavior, though these theories are not as well established as the corresponding Kosterlitz–Thouless theory in two dimensions. Monte Carlo simulations [10, 11] have yielded further support for this vortex loop picture of the phase transition. In the three–dimensional Heisenberg model there is also numerical evidence [12] for a phase transition mediated by point topological defects (monopoles), though this evidence has been questioned by other authors [13].

The role of topological defects at the nematic–isotropic phase transition poses intriguing questions. The defect structure in nematics is particularly rich and while sharing some similarities with the defect structures of the XY and Heisenberg models, there are significant differences due to the nature of the order parameter space. The local director $\hat{\mathbf{n}}$ of a nematic liquid crystal is defined as the average direction of alignment of a group of molecules. However, unlike the case of ferromagnets, the directions $\hat{\mathbf{n}}$ and $-\hat{\mathbf{n}}$ are equivalent. Thus, the order parameter space for nematics is P_2, the unit sphere with antipodal points identified. The stable topological defects [14] include monopoles and disclination lines. The monopoles are similar to the point defects of the Heisenberg model, though in the latter case, positive and negative topological charges of the same absolute value are distinct, whereas they are equivalent in the nematic [15]. While defect lines in the XY model can have any integer value with either positive or negative sign, one value of topological charge, $+1/2$, characterizes the entire class of stable line defects in nematics [15, 16]. All other half–integer valued lines, whether positive or negative, can be continuously deformed to a line with charge $+1/2$, and integer–valued lines can "escape in the third dimension" [17]. As in the XY model the disclination lines form closed loops or terminate on the surface of the sample because of the prohibitive energy cost of a free line end. However, whereas the XY model loops carry no net monopole charge, nematic disclination loops *can* (though all need not) carry monopole charge [18].

Not only is the classification of defects different in the nematic compared with the XY and Heisenberg models, but also the nature of the phase transition, first order in the former case and continuous in the latter. Lammert *et al.* [19] have argued that disclination lines are responsible for the first order nature of the nematic–isotropic (NI) transition. They developed and studied a lattice model of liquid crystals which allows for the suppression of the line defects while maintaining the presence of monopoles as in the Heisenberg model. As the defect lines are made more costly Lammert *et al.* [19] found that the transition between the ordered nematic phase (characterized by a nonzero disclination line tension) and the isotropic phase (characterized by zero line tension) becomes more weakly first order. At sufficiently large values of the core energy the transition splits into a pair of continuous transitions, and a new phase appears with no long–range nematic order but nonzero disclination line tension. In the extreme limit where the disclination lines are completely suppressed, their model reduces to the Heisenberg model with the expected continuous phase transition.

In this paper we report on a numerical study of topological defect behavior near the NI transition in the Lebwohl–Lasher (LL) lattice model [20] of liquid crystals which exhibits a weakly first–order phase transition (a weak first–order transition is characteristic of real experimental systems as well).

We also consider the defect behavior in a modified LL model which exhibits a strongly first–order transition. We find that two independent measures of the NI transition temperature, one the free energy and the other the distribution of disclination line segments, give almost identical values. By measuring the distribution of disclination loops as a function of their perimeter, we find evidence for the “blowout” of disclination loops at the transition, similar to the three–dimensional XY model. The disclination line tension in the modified LL model drops discontinuously to zero at the transition; in the case of the LL model, the transition is too weakly first–order to detect a similar discontinuity. We also measure the monopole charge of the loops and find in both the LL model and its modification that large loops and small loops adjacent to large loops have nonzero monopole charge, while small isolated loops do not. There appear to be no significant differences between the two models in the nature of the topological defects present.

In Sec. 4.2 we provide the details of our simulations and results, followed in Sec. 4.3 by our conclusions.

4.2 Simulations and Results

We performed Monte Carlo simulations on the Lebwohl–Lasher model, a lattice model of rotors with an orientational order–disorder transition. While it neglects the coupling between the orientational and translational degrees of freedom present in a real nematic liquid crystal, it is generally believed that this coupling does not play a significant role at the NI transition. With the absence of translational degrees of freedom the LL model is particularly well–suited for large–scale simulations of the transition. The model is defined by the Hamiltonian:

$$\mathcal{H}_{\mathcal{LL}} = -J \sum_{<ij>} P_2(\sigma_i \cdot \sigma_j) = -J \sum_{<ij>} \left\{ \frac{3}{2}(\sigma_i \cdot \sigma_j)^2 - \frac{1}{2} \right\} \tag{4.1}$$

where the sum is over all nearest-neighbors rotors situated on a cubic lattice. The long axes of the rotors are specified by the unit vectors σ_i), P_2 is the second–order Legendre polynomial, and J is a coupling parameter. The LL model has been intensively investigated using Monte Carlo techniques since its introduction [21, 22, 24, 25, 26, 27, 23]. The most complete numerical analysis of the NI transition in the LL model using the conventional single spin flip Metropolis algorithm was carried out by Zhang *et al.* [26] on systems up to a size of 28^3. However, the single spin flip algorithm is inefficient in the critical region and during the course of a simulation the system becomes trapped in one of the local minima corresponding to either the ordered or disordered phases. This difficulty can be overcome by using a cluster algorithm which is most efficient in the critical region and the system samples both local minima effectively. The first such algorithm for nematic liquid crystals was introduced by Kunz and Zumbach [28] to study the two–dimensional LL model. Their algorithm is a modification of the Wolff algorithm [29] for ferromagnetic systems, and greatly reduces critical slowing down. In an earlier publication [30] we used the Kunz–Zumbach algorithm to carry out a finite–size scaling analysis of the NI transition in the three–dimensional LL model with systems sizes up to 70^3 using the Ferrenberg–Swendsen reweighting technique [31].

Here we use the cluster algorithm to study the behavior of disclination lines and monopoles in the critical region. Following Ref. [19] we introduce a disclination line segment counting operator,

$$D_{ijkl} \equiv \frac{1}{2}\left[1 - \mathrm{sgn}\{(\sigma_i \cdot \sigma_j)(\sigma_j \cdot \sigma_k)(\sigma_k \cdot \sigma_l)(\sigma_l \cdot \sigma_i)\}\right] \tag{4.2}$$

which is unity if a disclination line segment pierces the lattice square defined by the four rotors $\sigma_i, \sigma_j, \sigma_k$ and σ_l. This method of locating disclination segments is mathematically equivalent to the method of Zapotocky *et al.* [32]. A disclination line segment can be considered as a bond on a cubic lattice dual to the original lattice of the rotors, and only an even number of bonds meet at a dual latticesite. Connecting the bonds to form disclination loops cannot be done in a unique way when four or six bonds meet at a site. To deal with this ambiguous case we followed the approach of Ref. [11] and chose a random pairing of the bonds. We thus traced the path of each disclination line through the system until the path crossed itself and formed a loop. The bonds of the loop were then eliminated from the dual lattice to avoid double counting when additional loops were traced.

We considered several measures of the nature of the disclination segments and loops, including the number of segments in the nematic and isotropic phases at coexistence, the distribution of loops

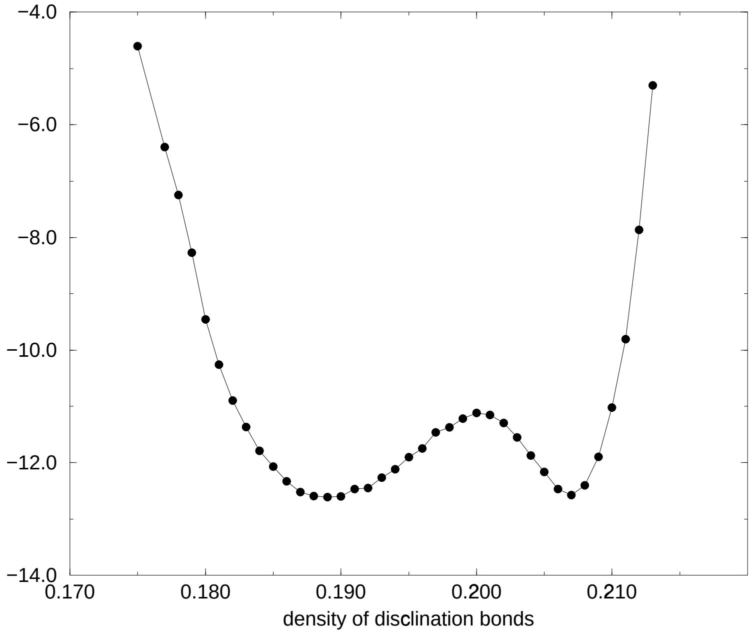

Figure 4.1: The logarithm of the distribution of disclination bond density in the Lebwohl–Lasher model, Eq. (4.1) for system size 70^3 at the NI transition temperature $T_{NI} = 1.1226$. The density is defined as the ratio of the number of disclination bonds to the total number of lattice bonds (3×70^3 in the present case). The solid line is a guide to the eye.

as a function of their perimeter, and the monopole charge of the loops.

We simulated a system of size 70^3 (with periodic boundary conditions) for 5×10^6 Monte Carlo steps (MCS) where one MCS corresponds to one cluster formation attempt and update of the spins comprising the cluster. Every 200 MCS we measured the total number of disclination line segments in the system and stored our data in a histogram. The logarithm of this histogram is shown in Fig. 4.1 at the temperature $T = 1.1226$ (temperatures measured in units of J/k_B) where the two wells have equal depth. The right–hand well corresponds to the isotropic phase (which we confirm by monitoring the nematic order parameter) and the left–hand well with fewer disclination line segments corresponds to the nematic phase. Varying the temperature by as little as 0.0001 yields wells of unequal depths. In our earlier work [30] we used the cluster algorithm to compute a histogram of the free energy (as a function of $E = \mathcal{H}_{\mathcal{L}\mathcal{L}}/N$, the energy per site). We found a double well structure for the free energy with equal well depths occuring at the temperature $T = 1.1226$, which we then identified as T_{NI}. Thus, the appearance of equal well depths in the histogram for the density of disclination line segments at the *same* temperature (to within our numerical accuracy) suggests that disclinations play a crucial role at the NI transition.

To further assess the role played by disclination loops at the transition we followed the approach used in Ref. [11] to study defect behavior at the three–dimensional XY transition, and calculated the perimeter distribution function $D(p)$ (the average number of loops with perimeter p). In Refs. [11] $D(p)$ was fit to the following form:

$$D(p) = A\ p^{-\alpha} \exp(-\epsilon(T)p/k_BT), \tag{4.3}$$

where $\epsilon(T)$ is the effective vortex line tension which is non zero at low temperatures. Thus, in the low temperature ordered phase vortex loops with large p are exponentially suppressed, and the length scale L_0 governing the typical perimeter size of the vortex loops is given by $L_0 = k_BT/\epsilon(T)$. At the critical temperature T_c of the XY model, $\epsilon(T)$ vanishes continuously and the distribution $D(p)$ has a power–law form. Consequently there will be a finite probability of having vortex loops which traverse the entire system and destroy the long–range order.

We computed $D(p)$ at the NI transition temperature $T_{NI} = 1.1226$ (identified by the two methods described above) and at two slightly lower temperatures. The results are shown in Fig. (4.2). We simulated the system for 5×10^6 MCS and computed $D(p)$ every 200 MCS to make sure that the successive configurations for bonds distribution are completely updated. Fitting our data to the form Eq. (4.2) yields $\alpha = 2.50 \pm 0.05$. For noninteracting loops (i.e. random walks) we expect $\alpha = 2.5$ exactly, whereas $\alpha > 2.5$ and $\alpha < 2.5$ for repulsive and attractive loop interactions respectively [33]. Unfortunately, we cannot distinguish among these three possibilities in our data.

While the relative depths of the wells appearing in the histogram Fig. (4.1) are sensitive to temperature variations as small as 0.0001 about T_{NI}, the distribution $D(p)$ is less sensitive. A plot of $D(p)$ at $T = 1.1225$, e.g., would be qualitatively similar to the appearance of $D(p)$ at T_{NI}, the upper curve in Fig. (4.2). However, deeper in the nematic phase at $T = 1.120$ (where the isotropic free energy well has disappeared) and $T = 1.10$, the behavior of $D(p)$ is different. Here one can

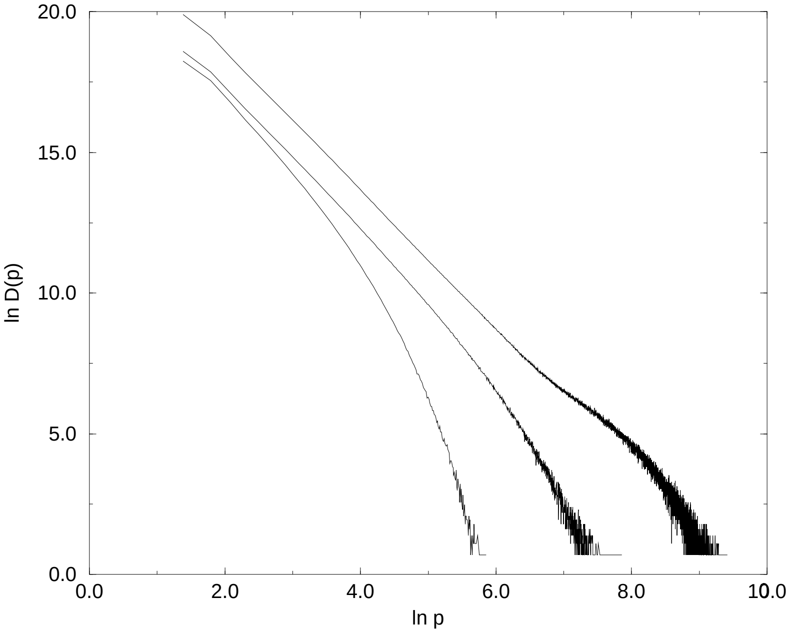

Figure 4.2: Log–log plot of the disclination loop distribution function $D(p)$ (Eq. (4.3)) in the Lebwohl–Lasher model, Eq. (4.1) for system size 70^3 at temperatures: $T_c = 1.1226$ (top curve), $T = 1.120$ (middle curve) and $T = 1.10$ (bottom curve).

clearly see an exponential decay at large values of p and the data can be fit to the form given in Eq. (4.3) with line tensions 0.003 and 0.026 at $T = 1.120$ and $T = 1.10$ respectively (these values were computed setting $\alpha = 2.5$).

The behavior of $D(p)$ shown in Fig. (4.2) is consistent with a "blowout" of disclination loops at the NI transition, similar to the behavior found in the three–dimensional XY model [11]. However, as indicated in the previous paragraph, $D(p)$ provides a less sensitive measure of the transition temperature compared to the histogram of the disclination line segments. The source of this drawback is the appearance of the bump at large perimeters in $D(p)$ in the neighborhood of T_{NI} which is a finite–size effect, arising from the nonzero probability of forming loops which wrap completely around the lattice due to the periodic boundary conditions. At high enough temperatures (in particular near the transition and above) there will be a sufficient number of disclination line segments present to form such loops.

The value of α for these loops is predicted to be unity for noninteracting loops in three dimensions [34]. The crossover in $D(p)$ from infinite system behavior (with $\alpha \simeq 2.5$) to the finite system behavior is expected to occur at a critical perimeter $p_c(L) \approx 1.5L^2/\pi$ for a system of size L [34]. Our results are in very good agreement with this scenario as shown in Fig. (4.2). The truncation of $D(p)$ at very large perimeters occurs because there are not enough disclination line segments (since we eliminated the previously marked ones) to construct loops with arbitrarily large perimeters. The deviation from the expected $\alpha = 2.5$ behavior for small p is due to the presence of the underlying lattice structure of the LL model.

We attempted to measure the jump in the effective line tension ϵ at T_{NI} in the LL model which is expected to occur because of the first order nature of the NI transition, in contrast to the continuous vanishing of ϵ observed in the XY model [11]. Naively one should compute $D(p)$ for temperatures in the vicinity of T_{NI} and extract the line tension $\epsilon(T)$ using Eq. (4.3) to fit the data. However, in practice this procedure is very difficult to carry out because the NI transition is weakly first order in the LL model and the jump in ϵ must be determined from the behavior of loops with very large perimeters. But loops with large perimeters wrap around the lattice as we described in the previous paragraph and thus appear in the “bump” region of Fig. (4.2) which cannot be fit with Eq. (4.3).

Another possibility would be to set the temperature to a value close to T_{NI}, calculate the nematic order parameter and then compute $D(p)$ separately in the isotropic and nematic phases. In principle the difference between the two distributions should give the jump in ϵ at the given temperature. However, again due to the very weak first order nature of the transition we found that each of these distributions was qualitatively similar to the critical distribution shown in Fig. (4.2). Thus at least for the systems sizes we have been able to study (less than or equal to 70^3), we have found it impossible to accurately measure the expected jump in the disclination line tension in the LL model.

To check our supposition that the disclination line tension should have a discontinuous jump at the first order NI transition, we considered a modified LL model, including a fourth–order Legendre polynomial P_4, which has been shown to make the NI transition more strongly first order [26, 35]. The modified Hamiltonian is given by :

$$\mathcal{H}' = -J \sum_{<ij>} P_2(\sigma_i \cdot \sigma_j) - J' \sum_{<ij>} P_4(\sigma_i \cdot \sigma_j) \tag{4.4}$$

This modified LL model was studied in Ref. [26] for a system of size 24^3 with $J'/J = 0.1$. We checked that the cluster algorithm produces free energy plots similar to those obtained in the latter reference where the single flip Monte Carlo algorithm was used.

We were able to measure the jump in the line tension for a system of size 50^3 with $J'/J = 0.3$ as shown in Fig. (4.3), finding a jump of approximately 0.0024 at the transition temperature $T = 1.2475$. Here we calculated $D(p)$ separately in the isotropic and nematic phases, with a production run of 10^7 MCS. We have been unable to carry out a finite–size scaling analysis of the jump because one has to choose the ratio J'/J large enough so that $D(p)$ exhibits behavior consistent with the form of Eq. (4.3) at large p in nematic phase; in particular with no “bump” as in Fig. (4.2). However, this choice of J'/J makes the transition more strongly first order and large systems can hardly overcome the resulting large free energy barrier. We also measured a histogram of the density of disclination line segments for the modified model and found behavior similar to that found in the LL model (see Fig. 4.1), namely equal well depths for this quantity at the *same* temperature where the free energy

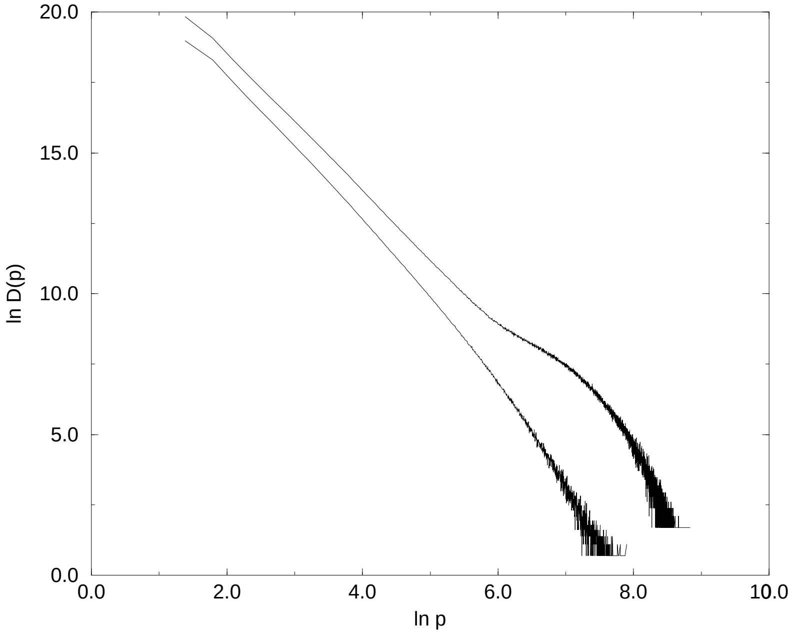

Figure 4.3: Log–log plot of the disclination loop distribution function $D(p)$ for the modified Lebwohl–Lasher model, Eq. (4.4), at its NI transition temperature $T = 1.2475$. The system size is 50^3 and the ratio of the couplings is $J'/J = 0.3$. The top curve (which has been displaced for the sake of clarity) and the bottom curve correspond to the isotropic and nematic wells of the free energy respectively. The jump in the disclination line tension is found to be 0.0024, and the straight portion of the isotropic data can be fit with a power–law of 2.50 ± 0.01 (see Eq. 4.3).

also exhibits two wells of equal depth.

As we discussed in Sec. 4.1, topological defects in nematics include not only disclination loops but monopoles as well, and furthermore the disclination loops can potentially carry monopole charge. To locate monopoles we used the prescription introduced by Berg and Lüscher [36] for the two–dimensional Heisenberg model which was subsequently extended by Lau and Dasgupta [12] to three dimensions. Each of the six faces of a lattice cube is divided into two equal area triangles by the face diagonal. The rotors σ_1, σ_2 and σ_3 at the three corners of each of the triangles are mapped to points on the order parameter sphere, forming spherical triangles. The area of each of the twelve spherical triangles formed by this mapping is then computed, with a sign given by $\mathrm{sgn}(\sigma_1 \cdot (\sigma_2 \times \sigma_3))$. The rotors on each triangle are numbered so that the circuit $1 \to 2 \to 3 \to 1$ corresponds to a counterclockwise rotation along the outward normal to the surface of the triangle. In performing this mapping we have assigned heads to the rotors such that the distance between the heads on the order parameter sphere is minimized, i.e., we use the “geodesic rule” [37, 38, 39] to effectively minimize the energy. For lattice cubes which are not pierced by disclination lines (and it is these cubes that we examine for monopole charge), the heads of all eight rotors at the corners of a cube can be simultaneously chosen to obey the geodesic rule without frustration. Thus, the angle between any pair of rotors at the corners of any of the twelve triangles will no greater than 90°. Finally, the monopole charge enclosed by the cube is given by the sum of the twelve signed areas of the spherical triangles divided by 4π.

Using this algorithm we examined all lattice cubes which are not pierced by disclination lines and found *no* monopoles, neither in the original LL model, Eq. (4.1), nor the modified model, Eq. (4.4). We searched for monopoles in the neighborhood of T_{NI}, deep in the nematic phase and at very high temperatures; in all cases no monopoles were located. This null result is not surprising given the topological arguments advanced by Hindmarsh [40] which yield a very low probability (of order 10^{-8}, compared with $\frac{1}{8}$ for the Heisenberg model) for the appearance of point monopoles in a nematic.

One way to measure the monopole charge of a disclination loop would be to apply the above algorithm to the surface of a group of lattice cubes which completely enclose a disclination loop. We have carried out this procedure for isolated loops of perimeter $p = 4$; none of these loops were found to carry monopole charge. It is difficult to carry out this procedure for larger loops, especially when two or more loops are entangled. In particular, when loops are entangled it is impossible to impose the geodesic rule simultaneously on all pairs of rotors. If we surround one loop completely with a set of lattice cubes, frustration will arise where the second loop pierces one of these lattice cubes. Instead we measured the local rotation vector $\mathbf{\Omega}$ of the four rotors surrounding each of the segments which form a disclination loop, and then summed these vectors along the entire length of the loop. If this sum is nearly zero, then the loop carries a nonzero monopole charge, because the set of rotors surrounding the entire loop will cover essentially the entire order parameter sphere [42, 43]. A simple example of this topology occurs in the case of a pure wedge loop where $\mathbf{\Omega}$ is everywhere tangent to the loop [41], and summing this vector around the loop yields zero identically; a simple example of a loop with zero monopole charge is a twist loop where $\mathbf{\Omega}$ is everywhere perpendicular to the plane of the loop. We measured the local rotation vector $\mathbf{\Omega}$ of the four rotors $\sigma_1, \sigma_2, \sigma_3, \sigma_4$ which lie at the corners of a lattice square pierced by a disclination line, by summing the vector cross product of each neighboring pair of rotors [44]:

$$\mathbf{\Omega} = (\sigma_1 \times \sigma_2) + (\sigma_2 \times \sigma_3) + (\sigma_3 \times \sigma_4) + (\sigma_4 \times (-\sigma_1)) \tag{4.5}$$

In writing this definition of $\mathbf{\Omega}$ we have chosen the heads of the rotors so that the neighboring pairs $\sigma_1, \sigma_2; \sigma_2, \sigma_3$ and σ_3, σ_4 satisfy the "geodesic rule" on the order parameter sphere. The remaining pair σ_4, σ_1 will not satisfy this rule because of the presence of the disclination line segment; thus we reflect σ_1 in the last term in Eq. (4.5), so that the vector products always involve pairs of rotors that satisfy the geodesic rule. To assign a unique sense to the circuit $1 \to 2 \to 3 \to 4 \to 1$, we arbitrarily assign a direction along the length of the disclination loop, and traverse the circuit in a counterclockwise sense along this direction. We note that the reflection of σ_1 in the last term of Eq. (4.5) guarantees that $\mathbf{\Omega}$ is independent of which of the four rotors is labeled 1.

Our results for the vector sum of $\mathbf{\Omega}$ along each disclination loop are shown in Fig. (4.4) for the LL model at its NI transition temperature $T_{NI} = 1.12279$ for a system of size 50^3. We use a smaller system size because the computation of this vector sum must be done using scalar code, whereas the cluster algorithm used above can be vectorized [30]. Similar results were obtained for the modified LL model. We note that all of the large loops with perimeters $p \geq 100$ are characterized by net rotation vectors which are nearly zero, suggesting that they carry nonzero monopole charge. We expect on energetic grounds that this charge will be unity rather than higher values. We have checked this supposition for a random sampling of loops finding that the rotation vectors cover a great circle on the order parameter sphere just once. Our data indicates that small isolated loops do not carry monopole charge. Rather the monopole charge is carried by large loops (with perimeters greater than 100) and small loops which touch larger ones.

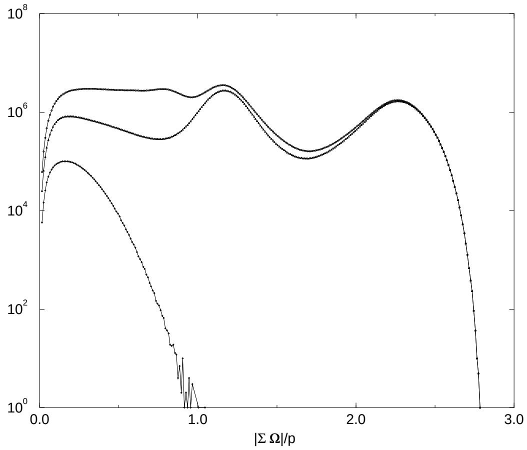

Figure 4.4: The distribution of $\mid \Sigma \ \mathbf{\Omega} \mid /p$, the magnitude of the vector sum of the rotation vector Ω, Eq. (4.5), along each disclination loop divided by its perimeter p, in the LL model of size 50^3 at T_{NI}. The top curve includes loops of all perimeters, the middle curve includes loops of $p = 4$ only, while the bottom curve includes only loops with $p > 100$. The rightmost peak appearing in the middle curve corresponds to isolated loops. Note that for a perfect wedge line segment piercing a square face of a lattice cube (i.e., a rotor configuration of the form $\sigma = (\cos\phi/2, \sin\phi/2)$, where ϕ is the azimuthal angle of the lattice site), $\mid \Sigma \ \mathbf{\Omega} \mid$ is given by $2\sqrt{2} \approx 2.8$.

4.3 Summary and Conclusions

In this project we have studied the properties of topological defects in two lattice models of the NI transition: the original Lebwohl–Lasher model (which exhibits a weakly first order transition) and a modified model with a more strongly first order transition. We have found evidence for the role played by disclination loops at the NI transition in both models. Namely, a histogram of disclination line segments collected over the course of the MC simulation shows a double well structure, and the wells are of equal depth at the *same* temperature where the free energy exhibits similar structure. We also find that the distribution $D(p)$ of disclination loops as a function of their perimeter exhibits power–law behavior at this temperature, consistent with the "blowout" of loops at the transition. However, $D(p)$ is a less sensitive measure of the transition temperature compared with the disclination segment histogram, due to finite size effects.

We have also searched for point monopoles in these models and measured the monopole charge of the disclination loops. We found no point monopoles, a result that may be reasonable on the basis of topological arguments [40]. However, we did find that nearly all of the large disclination loops carry monopole charge, while small isolated loops do not. Of particular interest is the result that the two models we studied, one with a weakly first–order transition and the other with a strongly first–order transition, showed no qualitative differences in their defect characteristics, other than the measurable jump in the disclination line tension in the latter model. In light of the results of Ref. [19] we find the similarities in the defect characteristics of the models we studied somewhat surprising. In Ref. [19] it was shown that suppressing disclination loops while leaving monopoles yields a more continuous NI transition. One might guess then that moving in the opposite direction to a model like that given in Eq. (4.4) which exhibits a strongly first–order transition one would find fewer monopole–like entities than in the LL model with its weakly first–order transition. While neither model has point monopoles, both appear to have similar densities of disclination loops with monopole charge, suggesting that monopole charge may not influence the strength of the first–order transition. We should also note that while our results suggest that disclination loops "blowout" at the NI transition in both models we considered, it is not clear from our study whether the transition is in fact defect–driven, or rather that some other mechanism drives the transition and the defects simply respond. Clearly more work on this very intriguing phase transition and the role played by topological defects would be of considerable interest.

Bibliography

[1] J. M. Kosterlitz and D. J. Thouless, J. Phys. C **6,** 1181 (1973).

[2] J. M. Kosterlitz, J. Phys. C **7,** 1046 (1974).

[3] D. R. Nelson and B. I. Halperin, Phys. Rev. B **19,** 2457 (1979).

[4] A. P. Young, Phys. Rev. B **19,** 1855 (1979).

[5] J. Villain, J. Phys. (Paris) **36,** 581 (1975).

[6] R. Savit, Phys. Rev. B **17,** 1340 (1978).

[7] L. Onsager, Nuovo Cimento Supp. **6,** 249 (1949).

[8] R. P. Feynman, in *Progress in Low Temperature Physics,* edited by C. J. Gorter (North–Holland, Amsterdam, 1955), Vol. 1, p. 17.

[9] B. Chattopadhyay, M. C. Mahato, and S. R. Shenoy, Phys. Rev. B **47,** 15159 (1993); G. A. Williams, Phys. Rev. Lett. **82,** 1201 (1999).

[10] G. Kohring, R. E. Shrock, and P. Wills, Phys. Rev. Lett. **57,** 1358 (1986).

[11] A. K. Nguyen and A. Sudbø, Phys. Rev. B **57,** 3123 (1998); Phys. Rev. B **60,** 15307 (1999).

[12] M. H. Lau and C. Dasgupta, Phys. Rev. B **39,** 7212 (1989).

[13] C. Holm and W. Janke, J. Phys. A **27,** 2553 (1994).

[14] P. de Gennes and J. Prost, *The Physics of Liquid Crystals* (Clarendon Press, Oxford, 1993).

[15] While monopoles in nematics are characterized by the absolute value of the integer charge, when monopoles with charges n and m coalesce, the resulting singularity can have charge of either $|n| + |m|$ or $||n| - |m||$ depending on the coalescence process; see G. E. Volovik and V. P. Mineev, Sov. Phys. JETP **45,** 1186 (1978).

[16] N. D. Mermin, Rev. Mod. Phys. **51,** 591 (1979).

[17] R. B. Meyer, Philos. Mag. **27,** 405 (1973).

[18] A. T. Garel, J. Phys. (Paris) **39,** 225 (1978); V. P. Mineev, Sov. Sci. Rev. **A2,** 173 (1980); H. Nakanishi, K. Hayashi, and H. Mori, Comm. Math. Phys. **117,** 203 (1988); H. Mori and H. Nakanishi, J. Phys. Soc. Jpn. **57,** 1281 (1988).

[19] P. E. Lammert, D. S. Rokhsar, and J. Toner, Phys. Rev. Lett. **70,** 1650 (1993), Phys. Rev. E **52,** 1778 (1995); J. Toner, P. E. Lammert, and D. S. Rokhsar, Phys. Rev. E **52,** 1801 (1995).

[20] P. A. Lebwohl and G. Lasher, Phys. Rev. A **47,** 4780 (1972).

[21] G. R. Luckhurst and P. Simpson, Mol. Phys. **47,** 251 (1982).

[22] U. Fabbri and C. Zannoni, Mol. Phys. **4,** 763 (1986).

[23] C. Zannoni, J. Chem. Phys. **84,** 424 (1986).

[24] G. Kohring and R. E. Shrock, Nucl. Phys. B **285,** 504 (1987).

[25] F. Biscarini, C. Zannoni, C. Chiccoli, and P. Pasini, Mol. Phys. **73,** 439 (1991).

[26] Z. Zhang, O. G. Mouritsen, and M. J. Zuckermann, Phys. Rev. Lett. **69**, 2803 (1992); Z. Zhang, M. J. Zuckermann, and O. G.Mouritsen, Mol. Phys. **80**, 1195 (1993).

[27] S. Boschi, M. P. Brunelli, C. Zannoni, C. Chiccoli, and P.Pasini, Int. J. Mod. Phys. C **8,** 547 (1997).

[28] H. Kunz and G. Zumbach, Phys. Lett. B **257,** 299 (1991); Phys. Rev. B **46**, 662 (1992). See also, S. Caracciolo, R. G. Edwards, A. Pelissetto and A. D. Sokal, Nuc. Phys. B **403,** 475 (1993).

[29] U. Wolff, Phys. Rev. Lett. **62,** 361 (1989).

[30] N. V. Priezjev and R. A. Pelcovits, Phys. Rev. E **63,** 062702 (2001).

[31] A. M. Ferrenberg and R. H. Swendsen, Phys. Rev. Lett. **61,** 2635 (1988).

[32] M. Zapotocky, P. M Goldbart, and N. Goldenfeld, Phys. Rev. E **51,** 1216 (1995).

[33] N. D. Antunes and L. M. A. Bettencourt, Phys. Rev. Lett. **81,** 3083 (1998).

[34] D. Austin, E. J. Copeland, and R. J. Rivers, Phys. Rev.D **49,** 4089 (1994).

[35] C. Zannoni, Mol. Cryst. Liq. Cryst. Lett. **49,** 247 (1979); C. Chiccoli, P. Pasini, P. Biscarini, and C. Zannoni, Mol. Phys. **65,** 1505 (1988); C. Chiccoli, P. Pasini, and C. Zannoni, Int. J. Mod. Phys. B **11** 1937 (1997).

[36] B. Berg and M. Lüscher, Nucl. Phys. B**190,** FS3, 412 (1981).

[37] T. Vachaspati, Phys. Rev. D **44,** 3723 (1991).

[38] S. Rudaz and A. M. Srivastava, Mod. Phys. Lett. A **8,** 1443 (1993).

[39] M. Hindmarsh,A.-C. Davis, and R. Brandenberger, Phys. Rev. D **49,** 1944 (1994).

[40] M. Hindmarsh, Phys. Rev. Lett. **75,** 2502 (1995).

[41] A. H. Windle, H. E. Assender, and M. S. Lavine, Proc. R. Soc. Lond. A **348,** 73 (1994).

[42] E. M. Terentjev, Phys. Rev. E **51,** 1330 (1995).

[43] M. Zapotocky and T. C. Lubensky, (unpublished).

[44] J. Hobdell and A. Windle, Liq. Cryst. **23,** 157 (1997).

Chapter 5

Coarsening Dynamics of Biaxial Nematic Liquid Crystals

In this chapter we study the coarsening dynamics of two and three dimensional biaxial nematic liquid crystals, using Langevin dynamics. Unlike previous work, we use a model with no a priori relationship among the three elastic constants associated with director deformations. We find a rich variety of coarsening behavior, including the simultaneous decay of nearly equal populations of the three classes of half–integer disclination lines. The behavior we observed can be understood on the basis of the relative values of the elastic constants and the resulting decay channels of the defects.

5.1 Role of topological defects in coarsening dynamics

Topological defects play an important role in the equilibration process following a quench from a disordered to an ordered phase ("coarsening dynamics"). Coarsening dynamics in nematic liquid crystals, particularly with uniaxial ordering, has been the subject of much active investigation in recent years in theory, experiments and simulations [1, 2, 3, 4], in part because of the rich defect structure of liquid crystals. On the other hand, relatively little attention (with the exception of the two–dimensional work of Ref. [2] has been paid to coarsening dynamics in biaxial liquid crystals, in

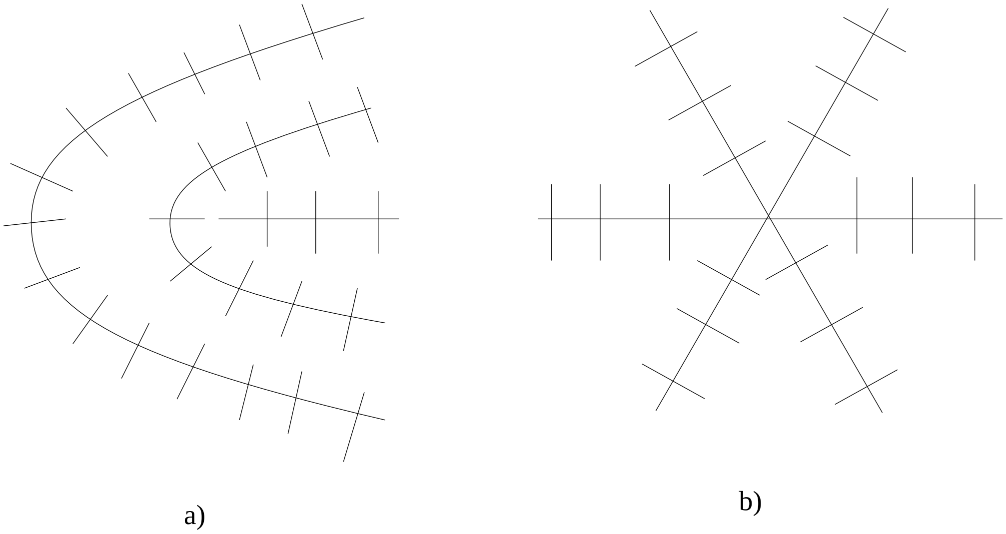

Figure 5.1: (a) Schematic illustration of a $\frac{1}{2}$ disclination line for biaxial nematics. Two directors rotate by 180° around the core of the line and the third one stays undistorted. (b) A disclination line of strength 1 is shown, where two out of three directors are rotated by 360°.

part because of the dearth of experimental realizations of biaxial liquid crystalline phases. However, biaxial nematics have many unusual topological features, which might be expected to influence their coarsening dynamics and thus warrant study. Biaxial nematics differ from their uniaxial counterparts in that they possess four topologically distinct classes of line defects (disclinations), while possessing no stable point defects (except in two dimensions where the line defects reduce to points) [5, 6]. The order parameter space for the objects with rectangular symmetry is $R = SO(3)/D_2$.

The classes of disclination lines are distinguished by the rotation of the long and short axes of the rectangular building blocks of the system. In the first three classes one of the three axes is uniformly ordered, while the remaining two axes rotate by 180° about the core of the defect as illustrated on Fig. (5.1a). The fourth class consists of 360° rotations of two of the three axes. The example of such a configuration is shown on Fig. (5.1b). The disclination lines form closed loops in three dimensions (with a single defect class per loop) or form a network where three lines, each from a different class meet at junction points [7]. The fundamental homotopy group of biaxial nematics is non–Abelian leading to a number of interesting consequences. E.g., the merging of two defects will depend on the path they follow, and two 180° disclinations of different types will be connected by a 360° "umbilical" cord after crossing each other [8].

5.2 Free Energy for Biaxial Nematic Liquid Crystals

Zapotocky *et al.* [2] studied coarsening dynamics in a two–dimensional model of biaxial nematics, utilizing a cell–dynamical scheme applied to a Landau–Ginzburg model, where the gradient portion of the energy was given by:

$$F_{grad} = \frac{1}{2} M (\partial_\alpha Q_{\beta\gamma})(\partial_\alpha Q_{\beta\gamma}). \tag{5.1}$$

Here M is a coupling constant, and $Q_{\alpha\beta}$ is the symmetric–traceless nematic order parameter tensor. Repeated indices are summed over; in the case of a two–dimensional nematic, α is summed over x and y, while β and γ are summed over x, y and z. Zapotocky *et al.* found that of the four topologically distinct classes of disclinations, only two classes (both corresponding to "half-integer" lines, i.e., 180° rotations) were present in large numbers at late times. Subsequently, Kobdaj and Thomas [9] showed within this one–elastic constant approximation that one class of half–integer disclinations is always energetically unstable towards dissociation into disclinations of the other two half–integer classes.

In this chapter we show that if one considers a more general gradient energy the coarsening dynamics of biaxial nematics is much richer than what occurs with the above simple model. In particular, with appropriate sets of parameters one can obtain a coarsening sequence with all three classes of half–integer disclinations present in nearly equal numbers even at late times, or a sequence with only one class of half–integer disclinations surviving until late times. When all three classes are present, the topology of the coarsening sequence in three dimensions is markedly different from the uniaxial case.

To understand why the model free energy of Eq. (5.1) is not general enough for coarsening studies, it is helpful to see what it yields for the director elastic constants. For biaxial nematics there are three directors which form an orthonormal triad of vectors $\mathbf{u}, \mathbf{v}, \mathbf{w}$ describing the alignment of the constituent "brick–like" molecules (see Fig. 5.2). The tensor $Q_{\alpha\beta}$ can be written in terms of the orthonormal triad as:

$$Q_{\alpha\beta} = S(w_\alpha w_\beta - \frac{1}{3}\delta_{\alpha\beta}) + T(u_\alpha u_\beta - v_\alpha v_\beta), \tag{5.2}$$

where S and T are respectively the uniaxial and biaxial order parameters. If we insert Eq. (5.2) into Eq. (5.1), we find [10]:

$$\begin{aligned} F_{grad} &= K_u[(\mathbf{u}\cdot\nabla\mathbf{v}\cdot\mathbf{w})^{\mathbf{2}}+(\mathbf{v}\cdot\nabla\mathbf{v}\cdot\mathbf{w})^{\mathbf{2}}+(\mathbf{w}\cdot\nabla\mathbf{w}\cdot\mathbf{v})^{\mathbf{2}}] \\ &+ K_v[(\mathbf{v}\cdot\nabla\mathbf{w}\cdot\mathbf{u})^{\mathbf{2}}+(\mathbf{u}\cdot\nabla\mathbf{u}\cdot\mathbf{w})^{\mathbf{2}}+(\mathbf{w}\cdot\nabla\mathbf{w}\cdot\mathbf{u})^{\mathbf{2}}] \\ &+ K_w[(\mathbf{w}\cdot\nabla\mathbf{u}\cdot\mathbf{v})^{\mathbf{2}}+(\mathbf{u}\cdot\nabla\mathbf{u}\cdot\mathbf{v})^{\mathbf{2}}+(\mathbf{v}\cdot\nabla\mathbf{v}\cdot\mathbf{u})^{\mathbf{2}}], \end{aligned} \tag{5.3}$$

where

$$\begin{aligned} K_u &= 2M(S+T)^2 \\ K_v &= 2M(S-T)^2 \\ K_w &= 8MT^2 \end{aligned} \tag{5.4}$$

Thus, there are three elastic constants K_u, K_v, K_w, each corresponding to one of the three classes of line defects. Each class corresponds to rotations of two of the three vector fields $\mathbf{u}, \mathbf{v}, \mathbf{w}$, about the defect core, with the third vector of the triad undistorted. We denote the classes as follows [6, 7]: C_u ($\mathbf{u}$ undistorted), C_w ($\mathbf{w}$ undistorted), and C_v ($\mathbf{v}$ undistorted). The energy of a defect in class C_i, $i = u, v, w$ is proportional to the elastic constant K_i. Note, however, that in the model specified by Eq. (5.1) only two of the three elastic constants are independent, as they are related as indicated in Eq. (5.4). In fact, the specific relationship among the three elastic constants gives rise, as shown in Ref. [9], to the presence of only two defect classes at late times. Irrespective of the values of S and T (M simply sets the overall scale of all three elastic constants), one of the three elastic constants is *always* greater than the other two, yielding a decay channel for the defect in the class with the largest elastic constant.

There is no symmetry reason to restrict our attention to the model free energy, Eq. (5.1). Even if we neglect the elastic anisotropy associated with bend, splay and twist distortions, a biaxial nematic should be described in general by three *independent* elastic constants, K_u, K_v and K_w [10]. In

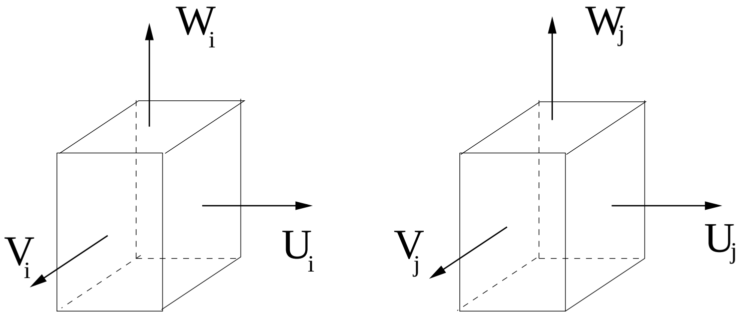

Figure 5.2: Two nearest neighbor rectangular blocks are illustrated with main symmetry axes being $\mathbf{u}, \mathbf{v}, \mathbf{w}$. The biaxial phase is characterized by long range order in all three axes.

terms of the order parameter tensor $Q_{\alpha\beta}$, this requires a term of third order in F_{grad}:

$$F_{grad} = \frac{1}{2}M(\partial_\alpha Q_{\beta\gamma})(\partial_\alpha Q_{\beta\gamma}) + LQ_{\alpha\beta}(\partial_\rho Q_{\alpha\gamma})(\partial_\rho Q_{\beta\gamma}), \tag{5.5}$$

which upon substituting Eq. (5.2) yields the elastic constants:

$$\begin{aligned} K_u &= 2(M(S+T)+LST)(S+T) \\ K_v &= 2(M(S-T)-LST)(S-T) \\ K_w &= 4(2M-LT)T^2 \end{aligned} \tag{5.6}$$

Because of the extra coupling constant L, there is no predetermined hierarchy among these elastic constants. Unlike the model of Eq. (5.1) it is now possible with appropriate choices of S, T and the ratio L/M to have all three elastic constants equal (which will give rise as we demonstrate below to a coarsening sequence with nearly equal populations of the three classes of half–integer defects), or have one constant smaller than the remaining two, yielding a coarsening sequence with only one class of defects at late times, or recover the behavior seen in Ref. [2].

5.3 Simulation Results

To simulate the coarsening dynamics of this general model of biaxial nematics, we consider its lattice analog introduced by Straley [11]. In this model the interaction between two biaxial objects located at sites i and j of a cubic lattice with orientations specified by the orthonormal triad $\mathbf{u}, \mathbf{v}, \mathbf{w}$ (see Fig. 5.2) is given by:

$$\begin{aligned} U_{ij} = -\frac{3}{2}\beta(\mathbf{w_i}\cdot\mathbf{w_j})^2 - 2\gamma[(\mathbf{u_i}\cdot\mathbf{u_j})^2 - (\mathbf{v_i}\cdot\mathbf{v_j})^2] - \\ \frac{\delta}{2}[(\mathbf{u_i}\cdot\mathbf{u_j})^2 + (\mathbf{v_i}\cdot\mathbf{v_j})^2 - \ (\mathbf{u_i}\cdot\mathbf{v_j})^2 - (\mathbf{v_i}\cdot\mathbf{u_j})^2]. \end{aligned} \tag{5.7}$$

This model has a phase diagram with two uniaxial phases, one with rodlike nematic order (alignment of the $\mathbf{w}$ vector field), one with discotic order (alignment of the $\mathbf{u}$ vector field) and a biaxial phase with alignment of all three vector fields [11, 12, 13].

The elastic constants emerging from Eq. (5.7) can be determined by considering the interaction between two objects which are aligned in turn along each of the three directions $\mathbf{u}, \mathbf{v}, \mathbf{w}$, with the results:

$$\begin{aligned} K_u &= \frac{3\beta}{2} - 2\gamma + \frac{\delta}{2} \\ K_v &= \frac{3\beta}{2} + 2\gamma + \frac{\delta}{2} \\ K_w &= 2\delta \end{aligned} \tag{5.8}$$

As in the continuum model Eq. (5.3), the parameters β, γ and δ give rise to three independent elastic constants. Stability requires that $3\beta + \delta > 4|\gamma|$, and $\beta, \delta > 0$.

We have simulated the coarsening dynamics associated with Eq. (5.7) using Langevin dynamics, expressing the three unit vectors $\mathbf{w}$, $\mathbf{u}$ and $\mathbf{v}$ in terms of Euler angles ϕ, θ and ψ. The equations of motion are given by :

$$\begin{aligned} \zeta\frac{\partial\phi_i}{\partial t} &= -\frac{\partial U}{\partial\phi_i} + R_\phi(t) \\ \zeta\frac{\partial\cos\theta_i}{\partial t} &= -\frac{\partial U}{\partial\cos\theta_i} + R_\theta(t) \\ \zeta\frac{\partial\psi_i}{\partial t} &= -\frac{\partial U}{\partial\psi_i} + R_\psi(t) \end{aligned} \tag{5.9}$$

where U is the sum of U_{ij} over the nearest–neighbors of site i, ζ is a damping coefficient and

$R_\phi(t), R_\theta(t)$ and $R_\psi(t)$ are uncorrelated random thermal noise sources. Each of the random variables R has a Gaussian distribution of variance $2k_B T\zeta/\delta t$ where k_B, T and δt are Boltzmann's constant, the temperature and the time step respectively. We measured time in units of β (choosing $\zeta = 1$), and used a timestep $\delta t = 0.0005$. A dynamical equation for $\cos\theta$ rather than θ must be used in order to reach the correct equilibrium states [14]. We verified that our dynamical equations led to the same phase diagram produced by Monte Carlo simulations [12, 13].

As in previous numerical studies of defect behavior [15, 16], we introduce a disclination line segment counting operator,

$$D^w_{ijkl} \equiv \frac{1}{2}[1 - \mathrm{sgn}\{(\mathbf{w}_i \cdot \mathbf{w}_j)(\mathbf{w}_j \cdot \mathbf{w}_k)(\mathbf{w}_k \cdot \mathbf{w}_l)(\mathbf{w}_l \cdot \mathbf{w}_i)\}] \tag{5.10}$$

which is unity if a disclination line segment pierces the lattice square defined by the four vectors $\mathbf{w}_i, \mathbf{w}_j, \mathbf{w}_k$ and $\mathbf{w}_l$. We define analogous operators D^u_{ijkl} and D^v_{ijkl} for the $\mathbf{u}$ and $\mathbf{v}$ vectors on this lattice square. In principle either two or none of the three operators should be unity for a given square, and thus we can assign the line segment to one of the classes C_u, C_v or C_w. In practice, we found a small number of squares where only one or all three operators were unity, an artifact of the discreteness of the underlying lattice. We obtained physically reasonable results by classifying the defects on the basis of the operators D^u_{ijkl} and D^w_{ijkl}, assuming that D^v_{ijkl} was unity only if *one* of the two former operators was unity. This procedure always yielded closed defect loops in three dimensions, a reasonable test of our algorithm. We determined the location of the integer–valued defects where either $\mathbf{w}$ or $\mathbf{u}$ (or both) rotate by ±360° degrees using the algorithm of Ref. [4] which provides an upper bound on these defects. We found very few integer–valued defects using this method, so a more accurate algorithm is not needed.

We quenched the system instantaneously from an initial configuration of random orientations of the three vectors $\mathbf{u}, \mathbf{v}, \mathbf{w}$ (i.e., a high temperature state) to zero temperature (a biaxially ordered state for all $\delta \neq 0$), and then let the system evolve in time according to the dynamical equations (5.9) monitoring the defect populations both visually and statistically. We studied the model in both two and three dimensions.

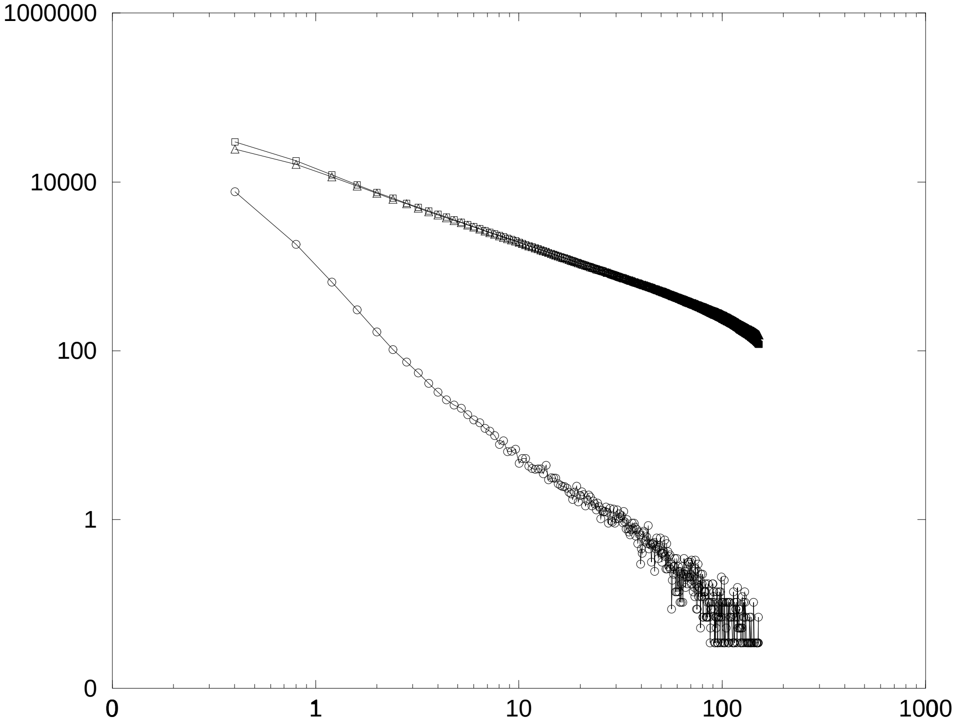

Figure 5.3: Log-log plot of the total line length of C_v ($\circ$), C_w ($\square$), and C_u ($\triangle$) class defects for system size 40^3, and parameters $\gamma = 1/2$, $\delta = 4\gamma^2/3 = 1/3$, as a function of time after the quench. The data has been averaged over 60 initial random configurations.

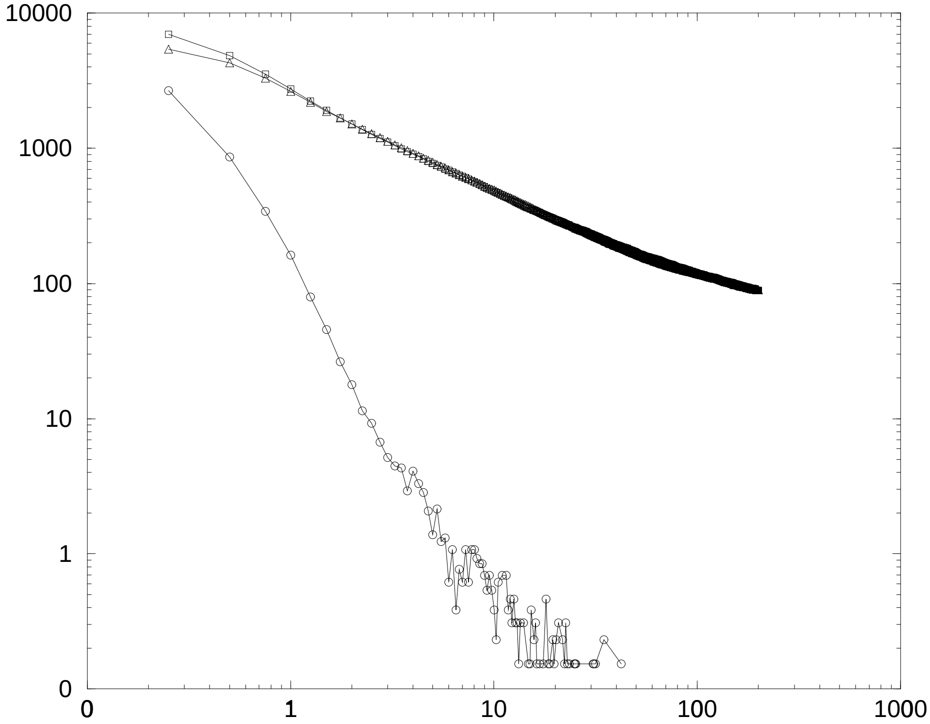

Figure 5.4: Log-log plot of the total number of vortices of C_v ($\circ$), C_w ($\Box$), and C_u ($\triangle$) class defects for system size 196^2, and parameters $\gamma = 1/2$, $\delta = 4\gamma^2/3 = 1/3$, as a function of time after the quench. The data has been averaged over 80 initial random configurations.

In agreement with our arguments above regarding the elastic constants, we found three qualitatively distinct types of coarsening behavior depending on the values of γ and δ (we set $\beta = 1$). For $\delta \ll 1$, and γ satisfying the stability requirement given after Eq. (5.8) defects of class C_w are energetically favorable compared to those of the other classes, and thus only these former defects survive until late times. For larger values of δ, but still less than 2γ (with $\gamma > 0$) we found defects belonging only to classes C_u and C_w, consistent with Eqs. (5.8), namely, $K_v > K_u + K_w$, and the results of Ref. [2]. This regime also includes the parameterization of Eq. (5.2) used in Refs. [12, 13], where $\delta = 4\gamma^2/3$ was chosen. In Fig. (5.4) we show the total number of vortices in two dimensional system as a function of time after the quench. These results are similar to those obtained in Ref. [2]. In Fig. (5.3) we show the total line length of defects in each of three classes as a function of time after the quench in three dimensions. In Fig. (5.5) we show a snapshot of the simulation cell late in the coarsening sequence. The C_v class defects have disappeared and the C_u and C_w class defects remain as nonintersecting closed loops. When $\gamma < 0$ and $\delta < 2|\gamma|$, we have $K_u > K_v + K_w$, and we found, consistent with this inequality, only defects of classes C_v and C_w at late times. We found no apparent line crossings, entanglements or junction points (the latter obviously would require three classes of defects). The two classes of loops appear to coarsen independently, as can be seen in the animations on our web site [17].

The most interesting and novel coarsening sequence occurs when $\gamma = 0$ and $\delta = 1$. For these parameters Eq. (5.8) implies that all three elastic constants are equal, and we found a coarsening sequence with nearly equal populations of the three defects. This behavior persists over a range of parameters $\delta \sim 1 \pm 0.5$ and $\gamma \sim 0 \pm 0.2$. In Fig. (5.8) we show the total number of vortices of each class in two dimensional system. Note the appearance of all three defect classes at late time after the quench. The coarsening sequence for these parameter values is particularly interesting in three dimensions. Soon after the quench a uniform network of junction points where three disclination lines (one from each of the three half–integer classes) meet is formed. These junction points are illustrated in Fig. (5.6) at late times after the quench.

The junction points are distributed in a nearly uniform fashion throughout the simulation cell,

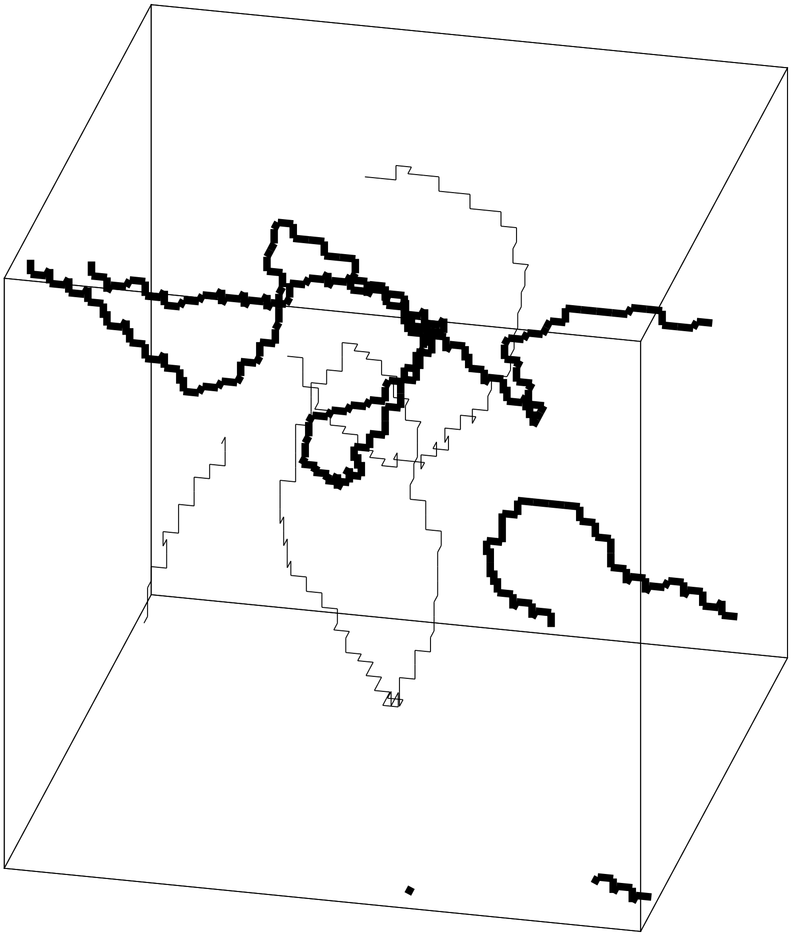

Figure 5.5: The configuration of C_u (thin line) and C_w (bold line) class defects for system size 40^3, and parameters $\gamma = 1/2$, $\delta = 4\gamma^2/3 = 1/3$, at dimensionless time 80 after the quench. Note that all C_v class defects have vanished at this late time, therefore C_w and C_u form nonintersecting loops which coarsen independently.

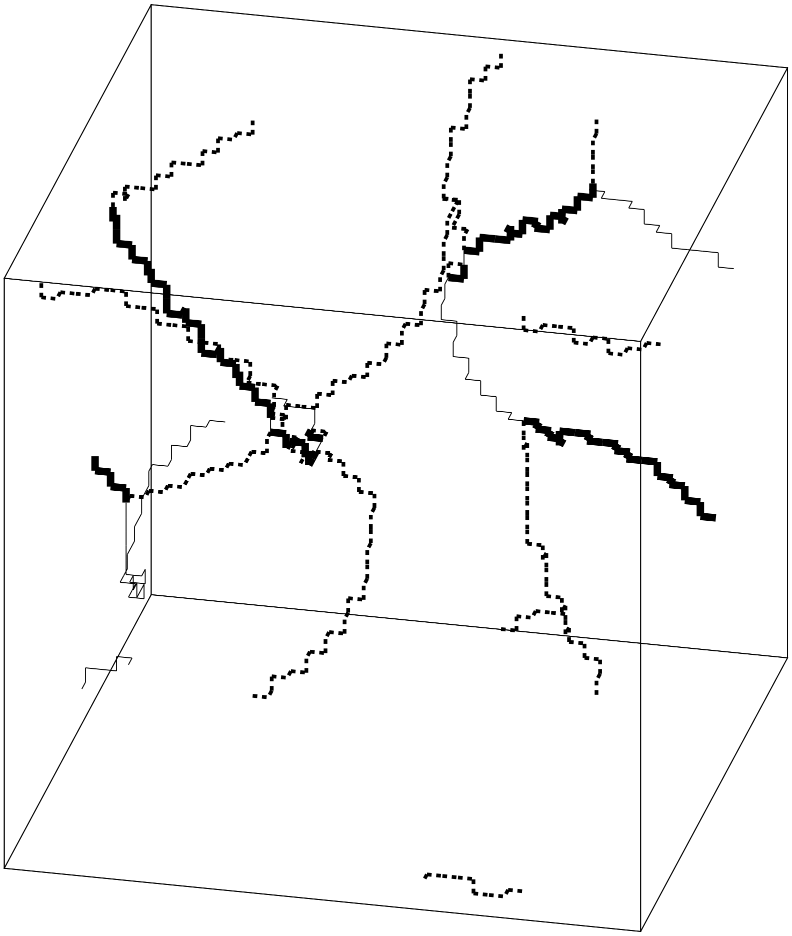

Figure 5.6: The configuration of C_u (thin line), C_v (dotted line), and C_w (bold line), class defects for system size 40^3, and parameters $\gamma = 0$, $\delta = 1$, at dimensionless time 60 after the quench.

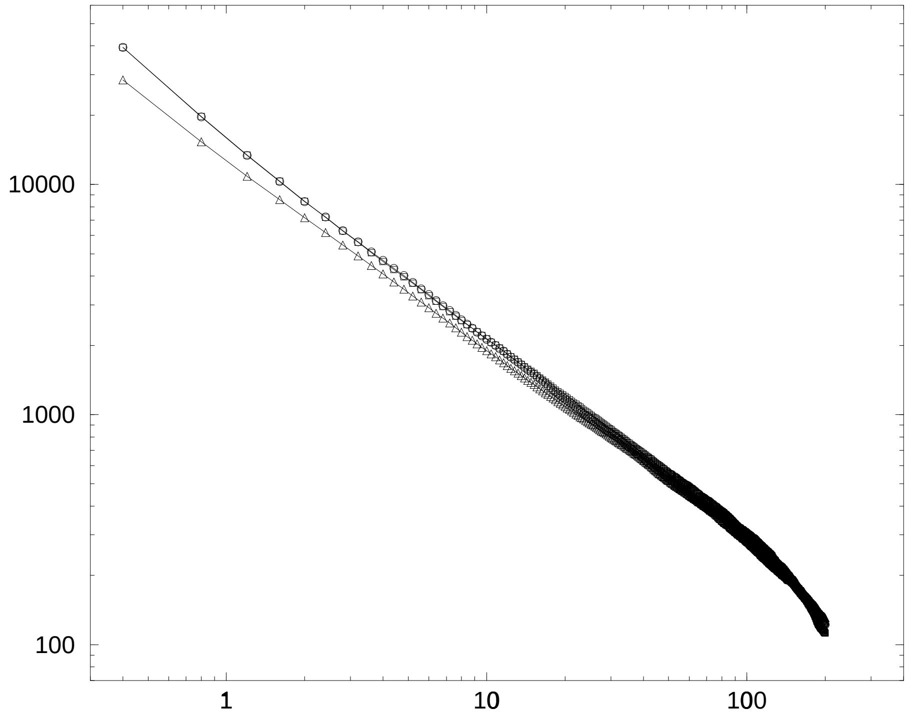

Figure 5.7: Log-log plot of the total line length of C_v ($\circ$), C_w ($\square$), and C_u ($\triangle$) class defects for system size 60^3, and parameters $\gamma = 0$, $\delta = 1$, as a function of dimensionless time after the quench. The data has been averaged over 40 initial random configurations. While in principle the population of the three classes of defects should be equal immediately after the quench, there is a small difference in these populations due to the numerical issues discussed in the text following Eq. (5.10).

and the distance between neighboring points grows on average with time [17]. The total line length of each of the three classes are nearly equal throughout the coarsening process (see Figs. 5.7).

When the distance between neighboring junction points becomes comparable with the size of the simulation cell (see Fig. 5.6), the coarsening process is impeded. The final annihilation of the disclination lines can only occur via the shrinkage of individual loops. The formation of loops requires that some pairs of neighboring junction points approach each other, shrinking the line joining them while possibly increasing the length of the other two disclination lines attached to the pair of junction points. Ultimately, the pair of junction points meet at a "pinch point", where four disclination line segments corresponding to two defect classes meet. Subsequently the four line segments dissociate

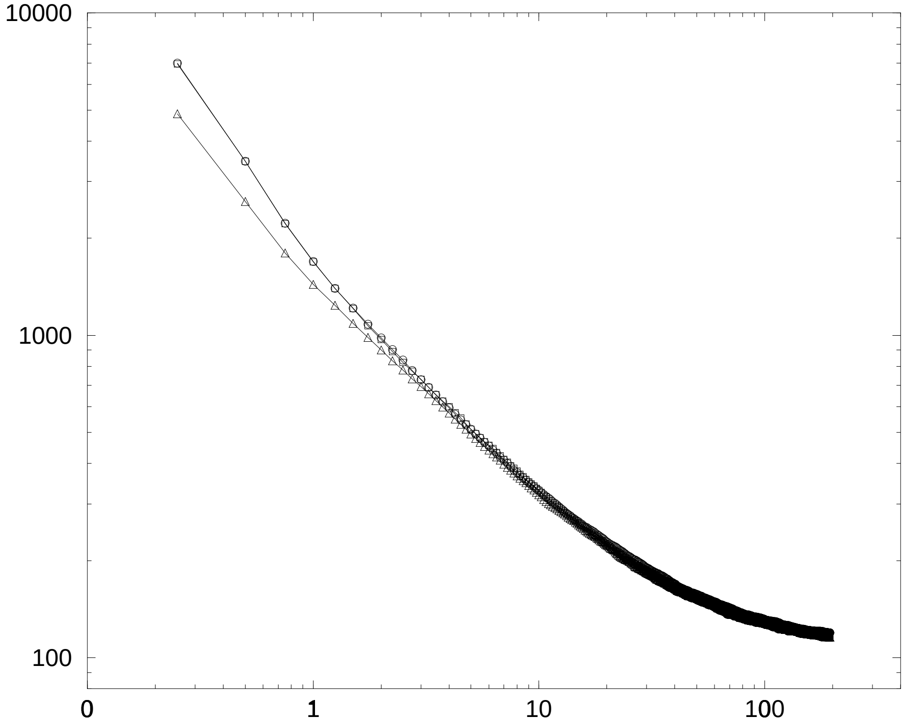

Figure 5.8: Log-log plot of the total number of vortices of C_v ($\circ$), C_w ($\Box$), and C_u ($\triangle$) class defects for system size 256^2, and parameters $\gamma = 0$, $\delta = 1$, as a function of dimensionless time after the quench. The data has been averaged over 60 initial random configurations. While in principle the population of the three classes of defects should be equal immediately after the quench, there is a small difference in these populations due to the numerical issues discussed in the text following Eq. (5.10).

into two nonintersecting single class line segments as can be seen in our animations [17]. When this process has occured a sufficient number of times, individual disclination loops are formed which then shrink independently.

In conclusion, we have shown that the coarsening dynamics of biaxial nematics is very rich, with late time behavior governed by either one, two or three classes of half–integer line defects, depending on the parameters of the system. When all three classes are present, a network of junction points is formed and a novel coarsening sequence occurs.

Bibliography

[1] R. E. Blundell and A. J. Bray, Phys. Rev. A **46**, R6154 (1992).

[2] M. Zapotocky, P. M. Goldbart, and N. Goldenfeld, Phys. Rev. E **51**, 1216 (1995).

[3] I. Chuang, B. Yurke, A. N. Pargellis, and N. Turok, Phys. Rev. E **47**, 3343 (1993).

[4] J. L. Billeter, A. M. Smondyrev, G. B. Loriot, and R. A. Pelcovits, Phys. Rev. E **60**, 6831 (1999).

[5] G. Toulouse, J. Phys. Lett. (Paris) **38**, L67 (1977).

[6] N. D. Mermin, Rev. Mod. Phys. **51**, 591 (1979).

[7] T. De'Neve, M. Kleman, and P. Navard, J. Phys. II (France) **2**, 187 (1992).

[8] V. Poenaru and G. Toulouse, J. Phys. (Paris) **8**, 887 (1977).

[9] C. Kobdaj and S. Thomas, Nucl. Phys. B **413**, 689 (1994).

[10] S. Sukumaran and G. S. Ranganath, J. Phys. II (France) **7**, 583 (1997).

[11] J. P. Straley, Phys. Rev. A **10**, 1881 (1974).

[12] G. R. Luckhurst and S. Romano, Mol. Phys. **40**, 129 (1980).

[13] F. Biscarini, C. Chiccoli, P. Pasini, F. Semeria, and C. Zannoni, Phys. Rev. Lett. **75**, 1803 (1995).

[14] C. Goze, Ricardo ParedesV., Carlos VasquezR., Ernesto MedinaD., and A. Hasmy, Phys. Rev. E **63**, 042701 (2001).

[15] P. E. Lammert, D. S. Rokhsar, and J. Toner, Phys. Rev. E **52**, 1778 (1995).

[16] N. V. Priezjev and R. A. Pelcovits, Phys. Rev. E **64**, 031710 (2001).

[17] http://www.physics.brown.edu/Users/faculty/pelcovits/biaxial/

Chapter 6

Summary and Future Directions

In this Thesis we have presented the results of simulation studies of nematic liquid crystals using Monte Carlo and molecular dynamics techniques.

In collaboration with Gregor Skačej and Professor S. Žumer at University of Ljubljana we investigated the problem of anchoring at a free surface of a nematic liquid crystal using Monte Carlo simulations. To estimate the corresponding extrapolation length, we impose a bend deformation in a hybrid cell–like nematic sample. The simulation is based on a simple hexagonal lattice model with nematic particles interacting via the spatially anisotropic modified induced dipole–induced potential. We measured the extrapolation length and compared our approach with the experiment.

Even more challenging are off–lattice simulations of a liquid crystalline systems. We have chosen a fluid of Gay–Berne particles to study the defects structure and their time evolution. Fluid simulations will allow us ultimately to study the effects of hydrodynamics on dynamics of defects and investigate the variety of defects in smectics, including dislocations and focal conics. We have developed a method to track monopoles in off–lattice models. It works as follows. First generate a Delaney triangulation of the system of Gay–Berne particles which creates a network of tetrahedra filling the MD cell. Next choose a sphere at an arbitrary point and construct a surface of outward laying faces of inner tetrahedras similar to the surface of a soccer ball. Then compute the signed areas of the spherical triangles on the order parameter sphere which are mapped from the directors on the surface triangles of the collection of tetrahedra and calculate the integer monopole charge. We have successfully tested the algorithm on a large systems with artificial monopole configuration inserted. The ideas involved in this approach will also serve as a basis for how we plan to locate screw and edge dislocations in smectics.